Chemical Science

ROYAL SOCIETY OF CHEMISTRY

REVIEW

View Article Online
View Journal | View Issue

Cite this: *Chem. Sci.*, 2025, **16**, 21745

Bridging MOF properties to 3D printing: a framework for electrochemical energy storage architectures with synergistic porosity-ion dynamics

Chenfei Zhou,[a] Huijie Zhou,*[ab] Xinyu Qin,*[a] Shunyu Gu,[a] Mengyao Zhang,[a] Jifan Chen,[ac] Lingfeng Zhai[ad] and Huan Pang *[ab]

Metal–organic frameworks (MOFs) offer exceptional tunability, high porosity, and chemical versatility, positioning them as highly promising candidates for electrochemical energy storage, particularly batteries and supercapacitors. However, their integration into 3D printingplatforms remains hindered by rheological limitations and structural fragility. This review introduces a property-oriented design framework that strategically aligns key MOF attributes—mechanical flexibility, electrical conductivity, and thermal stability—with specific 3D printing techniques, including Direct Ink Writing (DIW), Fused Deposition Modeling (FDM), Digital Light Processing (DLP), and Selective Laser Sintering (SLS). By leveraging ligand engineering and composite formulation, MOF mechanical–electrochemical properties can be tuned to meet the requirements of various AM methods. This enables the fabrication of advanced battery and supercapacitor electrodes featuring hierarchical porosity, optimized ion transport, and mechanical robustness. We systematically review MOF precursor formats (inks, filaments, resins, powders) and post-processing strategies such as *in situ* growth and interfacial coating. Breakthrough applications in supercapacitors and batteries demonstrate the transformative potential of this integrated approach. Collectively, this work establishes a design paradigm that bridges porous material chemistry with advanced manufacturing for next-generation electrochemical energy storage architectures.

Received 14th August 2025
Accepted 5th November 2025

DOI: 10.1039/d5sc06210a

rsc.li/chemical-science

1 Introduction

As global demand for sustainable energy resources continues to grow, conventional energy supplies are increasingly insufficient to meet modern societal needs.[1,2] Consequently, the development of advanced materials and manufacturing techniques for high-performance electrodes has become a primary research focus in electrochemical energy storage (EES).[3] Metal–organic frameworks (MOFs), first reported by Yaghi and Li[4] in 1995, are porous crystalline materials synthesized through the coordination of metal ions/clusters with organic ligands.[5–7] MOFs have since emerged as a prominent class of materials ex5tensively utilized in various industries, including EES,[8–15] gas storage and separation,[16–20] catalysis,[13,21,22] and drug delivery.[23] However, the intrinsically poor conductivity and mechanical fragility of MOFs limit their direct use as electrodes. To address this, recent research has focused on forming conductive composites by integrating MOFs with carbon materials, conductive polymers, or metal oxides, which significantly improve their electrochemical performance.[24–29]

Electrodes play a pivotal role in determining the overall performance of EES devices by governing key metrics such as capacity, stability, and energy efficiency.[30–34] Traditional manufacturing methods, such as physical and chemical deposition, have limited control over the porosity and density of electrode structures, which limits ion transport and exposure of active surface area.[35,36] Furthermore, these techniques often require specific chemical environments and complex processing steps, restricting scalability and reproducibility. In contrast, the development of customizable electrodes provides greater design flexibility and can offer better electrochemical performance for the next generation of energy storage systems.

Extensive research has explored the application of 3D printing in the fabrication of EES devices, offering enhanced design flexibility and functional performance. This technique enables the precise construction of complex device geometries, from planar to three-dimensional spatial structures, with ease.[37–43] 3D printing provides a novel approach to producing

[a]*School of Chemistry and Materials, Yangzhou University, Yangzhou, Jiangsu, 225009, P. R. China. E-mail: huanpangchem@hotmail.com*
[b]*Institute of Technology for Carbon Neutralization, Yangzhou University, Yangzhou 225127, Jiangsu, PR China. E-mail: huanpangchem@hotmail.com*
[c]*School of Chemistry and Chemical Engineering, Chongqing University of Science and Technology, Chongqing, 401331, P. R. China*
[d]*School of Environmental Science, Nanjing Xiaozhuang University, Nanjing, Jiangsu, 211171, P. R. China*

EES devices from the macro to the nanoscale. When nanomaterials are incorporated into 3D-printed electrodes, their electrochemical activity can be significantly enhanced. Compared to traditional electrode fabrication methods, 3D printing offers fine control over electrode thickness, internal porosity and density, all of which are critical parameters for optimizing ion transport and energy storage performance. The excellent process adaptability and geometric precision of 3D printing also allow for the integration of diverse functional materials. The introduction of nanomaterials can greatly promote the manufacturing process of EES is possible to easily construct highly complex device shapes from flat to three-dimensional spatial structures through various 3D printing technologies.[44–52] Moreover, 3D printing facilitates cost-effective and eco-friendly production for EES devices through simplified, one-step 3D printing, minimized material waste and energy consumption relative to conventional techniques.[53,54] However, compared to other materials, MOFs present greater challenges for direct 3D printing.[55–58] Their inherently unsuitable rheological properties often impede smooth extrusion through syringes, while their tendency to entangle, sinter, or cure improperly can result in cracking in printed electrodes.[59–62] To overcome these limitations, recent advances have enabled MOFs to be processed into four distinct pre-printing formats: (1) functional inks for Direct Ink Writing (DIW), (2) polymer-MOF composite filaments for Fused Deposition Modeling (FDM), (3) photosensitive MOF-resin hybrids compatible with Digital Light Processing/Stereolithography Apparatus (DLP/SLA), and (4) sinterable MOF-polymer powders for Selective Laser Sintering (SLS). Crucially, post-printing strategies—such as *in situ* MOF growth on 3D scaffolds and interfacial coating—have emerged to circumvent ink limitations while enhancing active site accessibility.[63–65]

While existing reviews catalog general 3D printing approaches for MOFs, a critical gap persists: there is no systematic framework that links MOF physicochemical properties (flexibility, conductivity, and thermal stability) to tailored printing techniques and post-processing protocols. This review addresses this gap by introducing a property guided manufacturing paradigm. We begin by classifying conductive MOFs according to their key physical and electrochemical characteristics and then map these categories to optimal printing strategies (*e.g.*, flexible MOFs → DIW with self-healing binders; thermally stable MOFs → high-temperature SLS). Furthermore, we dissect how synergistic structure–property–design relationships enable the fabrication of customized electrodes with hierarchical porosity, accelerated ion transport, and effective suppression of dendrite formation. By critically assessing recent breakthroughs in MOF-based supercapacitors, Li/Zn-ion batteries, and hybrid systems, this work not only benchmarks current achievements but also outlines a roadmap for next-generation energy devices that leverage 3D printing's geometric versatility and multifunctional integration capabilities (Fig. 1).

2 Structural regulation of MOF printing adaptability

2.1 Rheology and flexibility design

Flexible MOFs impart 3D printing inks with suitable rheological properties and structural stability throughout the printing process. Additionally, their functionalization potential allows inks to be tailored for specific applications, such as catalysis and conductivity.[66] Furthermore, flexible MOFs offer notable advantages in mechanical performance and functional versatility (Fig. 2). For instance, An *et al.*[67] pioneered a solvothermal

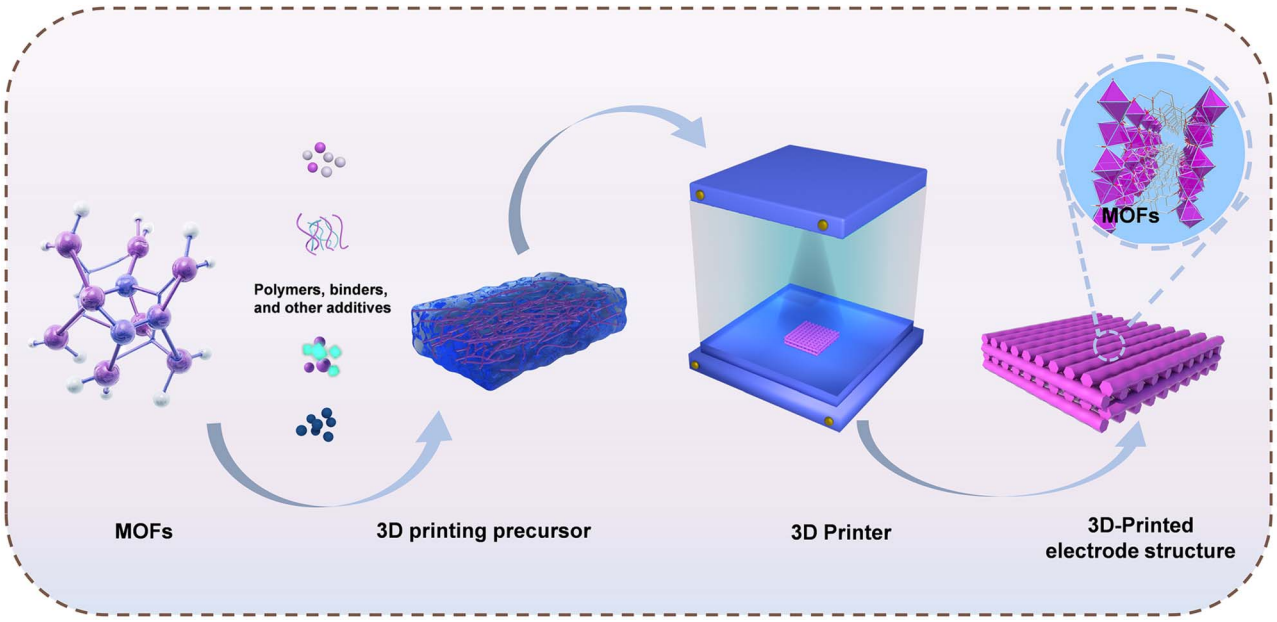

Fig. 1 The strategy for preparing mof into 3D printing precursors and the 3D printing schematic diagram.

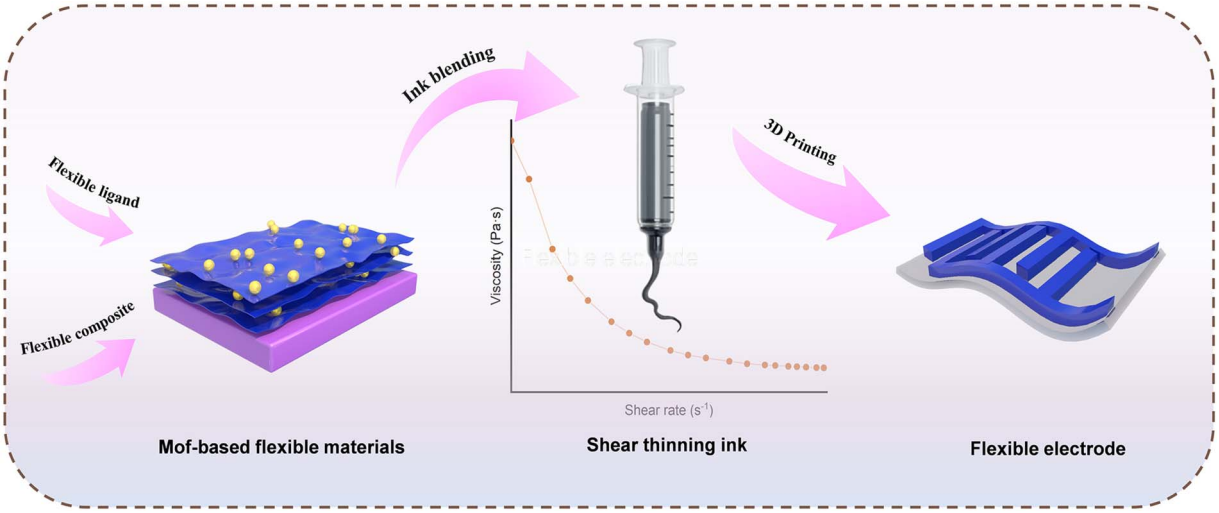

Fig. 2 Schematic illustration of MOF-based flexible materials for fabricating flexible electrodes *via* 3D printing of shear-thinning ink.

synthesis route using 3,3′,5,5′-tetramethyl-4,4′-bipyrazole and nickel(II) chloride hexahydrate to construct a flexible MOF with dynamic responsiveness, which served as an effective electrode material (Fig. 3a). This structural flexibility established a groundwork for subsequent studies and inspired Tian *et al.*[68] to develop a breakthrough design strategy. By integrating flexible molecular units with rigid building blocks at the molecular level, they synthesized multi-walled MOF architectures with hierarchical channels and multiresponsive capabilities (Fig. 3b). Such "rigidity-flexibility synergy" enabled reversible lattice deformations of up to 15% while maintaining structural integrity, creating an ideal platform for efficient ion transport within electrochemical systems.

The rheological properties of MOF-based inks, including viscosity (η), shear rate ($\dot{\gamma}$), and Reynolds number (Re), critically influence printability and structural fidelity.[69,70] Moderate

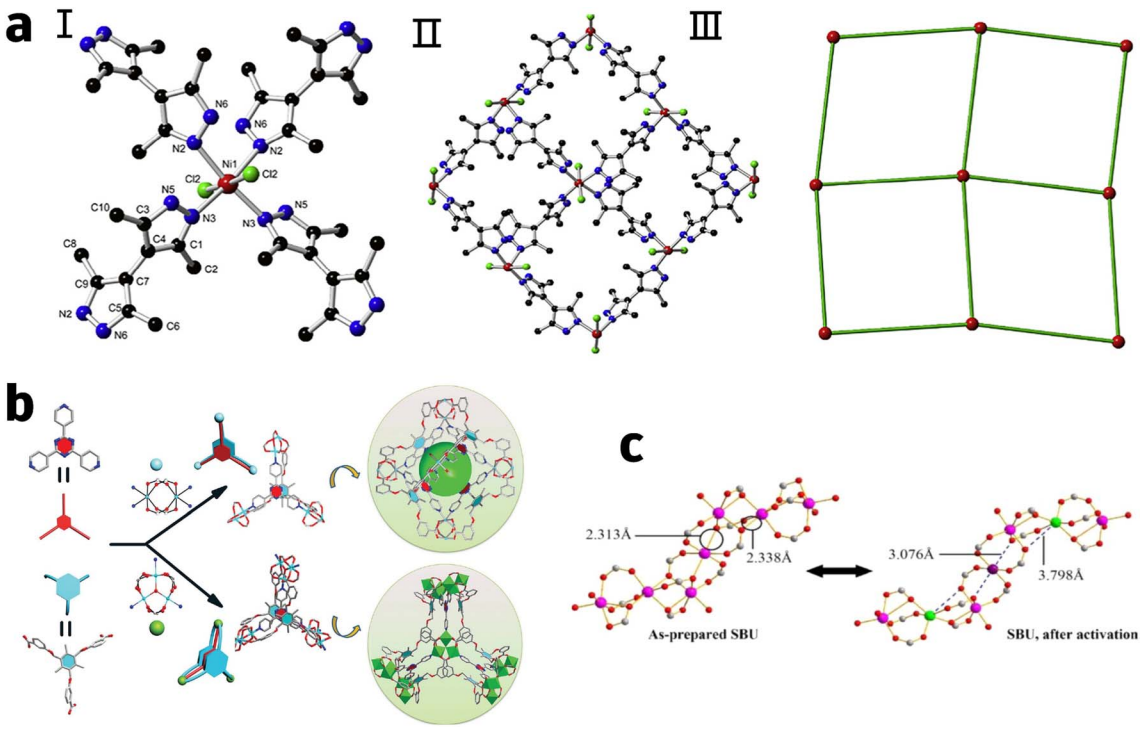

Fig. 3 (a) MOF (Ni–Me4bpz) crystal structure illustration shows: (I) Coordination pattern; (II) Flat conformation; (III) SQL-type network. Element color coding: Ni (red), Cl (green), N (blue), C (black). (b) Rationally engineered composite building blocks featuring dual- and triple-layer configurations. (c) During the structural distortion, some Mn2+ cations experienced a reduction in coordination: the violet centers decreased from six to four, while the green centers dropped from six to five. Dashed lines highlight the bonds that were broken.

viscosity (102–104 mPa s) and shear-thinning behavior enable smooth extrusion and rapid shape recovery. In addition to viscosity, the balance between the storage modulus (G') and loss modulus (G'') is a crucial factor governing the printability of MOF-based inks. The storage modulus (G') reflects the elastic or solid-like behavior, whereas the loss modulus (G'') represents the viscous or liquid-like response.[71,72] For printable inks, an optimal viscoelastic window is achieved when G' is slightly higher than G'' (typically $G'/G'' = 1.2–10$) at low shear rates, indicating a predominantly elastic network that can retain its shape after extrusion while still being able to flow under applied stress.[73] Re values below 1 indicate laminar flow, promoting uniform deposition, while excessively low viscosity or high Re can cause structural collapse or flow instability. Optimizing solvent composition, particle loading, and binder content is therefore essential to achieve a balance between flowability, shape retention, and mechanical flexibility, ensuring precise 3D printing and stable electrochemical performance of MOF-based electrodes.[74]

The growing research momentum has been further intensified by mechanistic revelations. Zhang *et al.*[75] discovered a "bipolar charging" mechanism while investigating the solid-state aelectrochemical process of MOFs. For example, in lithium-ion batteries, this mechanism facilitates the simultaneous intercalation of lithium ions and larger anions into the pores of the MOF during a single redox cycle. Both species actively participate in the electrochemical reaction, thereby effectively boosting the overall capacity of the system (Fig. 3c).

Selecting flexible ligands is an effective approach for synthesizing of flexible MOFs. During synthesis process or upon exposure to external stimuli, these ligands can adapt their conformations to accommodate changes in the coordination environment of metal centers, thereby imparting structural flexibility to the MOFs. For example, Wang *et al.*[76] successfully synthesized a novel isostructural Ni-based MOF, $[Ni_2(TATB)_2(L)_2(H_2O)]$, where L represents flexible N-donor ligands bid (1,10-diazadecane) or btd (1,10-bis(triazole)decane), and TATB refers to the deprotonated form of 4,4′,4″-*s*-triazine-2,4,6-tricarboxylic acid (H_3TATB) (Fig. 4a). The resulting flexible MOF can be directly applied as an electrode material for SCs. Building on this ligand-driven design principle, Lai *et al.*[77] employed quinone-based ligands to synthesize two MOFs, namely the one-dimensional 1D linear zinc anthraquinone-2,3-dicarboxylate coordination polymer and the 2D manganese anthraquinone-2,3-dicarboxylate coordination polymer through a simple hydrothermal reaction. The high flexibility of quinone-based organic ligands endows MOFs with adaptability, enabling them to deliver robust performance when applied in lithium-ion batteries (Fig. 4b).

Expanding functional versatility, Wu *et al.*[78] engineered a 2D conductive MOF (Cu-BHT) in which ligand flexibility coexists with a high density of redox-active sites and superior electronic

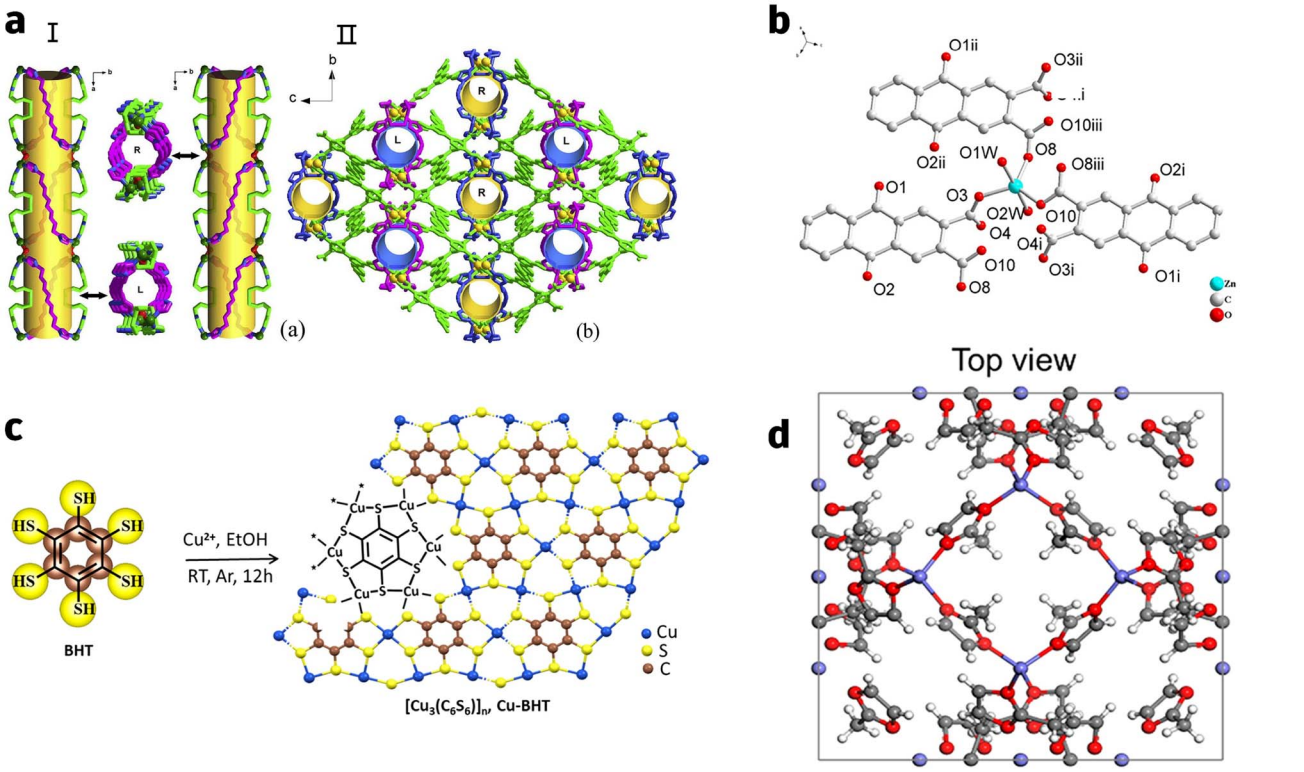

Fig. 4 (a) (I) Diagram illustrating left- and right-handed helical channels oriented along various directions. (II) A three-dimensional framework featuring intertwined helical channels of both left- and right-handed twists. (b) Coordination environment diagram for the structural unit of MnAQDC ($MnC_{16}H_{10}O_8 \cdot 2H_2O$), with the following symmetry operations applied: (I) $(1 + x, y, z)$, (II) $(1 - x, 2 - y, 2 - z)$, (III) $(2 - x, 1 - y, 2 - z)$. (c) Synthesis process of the 2D Cu-BHT MOF. (d) Planar projection of the tuned C-ZIF-8 crystal lattice.

conductivity. This combined functionality granted lithium-ion batteries (LIBs) exceptional power density and ultra-long cycling stability during charge/discharge process (Fig. 4c). Extending this design concept to membrane technology, He *et al.*[79] developed a flexible MOF-based membrane with excellent mechanical flexibility. The highly uniform pore structure of the MOF particles facilitates homogeneous lithium-ion flux, fundamentally suppressing lithium dendrite growth. Additionally, the MOF composite membrane serves as an effective barrier against polysulfide shuttling, enabling Li–S coin cells to achieve ultra-long cycling life.

Advancing composite architecture design, Ma *et al.*[80] hybridized MOFs with bacterial cellulose to fabricate a BC@ZIF-8 aerogel sponge. This material combined MOF porosity (<0.03 g cm−3 density, hierarchical pores) with the mechanical resilience of BC, resulting in exceptional mass transfer efficiency for adsorption/desorption processes. Notably, its heavy metal ion adsorption capacity highlights its crossover potential in environmental remediation. Reimagining anode protection, Xiang *et al.*[81] engineered a continuous amorphous MOF (AMOF) layer that outperformed crystalline counterparts in stabilizing zinc anode. The grain boundary-free AMOF coating effectively suppresses dendrite formation and hydrogen evolution while promoting high Zn2+ migration (tZn2+ = 0.75). Impressively, Zn@A-ZIF-8 symmetric cells demonstrated 7900-hour stability (<40 mV overpotential) and maintained performance for 5500 cycles at 10 mA cm−2. Even under 180° bending, the system retained its mechanical flexibility, underscoring the AMOF's viability for deformable electronics (Fig. 4d).

Flexible conductive MOFs are emerging as highly versatile materials with considerable potential in energy storage, environmental remediation, and other electrochemical applications. The design of such MOFs typically relies on the strategic selection of flexible ligands capable of adapting their conformations to the coordination environment, thereby enhancing both mechanical flexibility and electrochemical performance. For instance, flexible N-donor ligands, quinone-based linkers, and hybrid structures that integrate rigid and flexible components can simultaneously improve porosity, conductivity, and stability. These attributes make flexible MOFs particularly attractive for use in LIBs, where they help suppress dendrite growth, promote ion transport, and extend cycle life. In SCs, their high surface area and inherent flexibility facilitate rapid charge–discharge processes.

2.2 Thermal stability modulation

Thermally stable MOFs are attracting increasing interest for application in 3D printing inks, where their unique properties contribute to both the rheological behavior and structural integrity of the printed materials.[82,83] The inherent thermal stability of these MOFs ensures that the inks maintain consistent performance under variable temperatures throughout the printing process, which is an essential factor for achieving high precision and durability in 3D-printed objects (Fig. 5). Additionally, the functionalization potential of thermally stable MOFs allows inks to be customized for specific applications, such as catalysis, improved conductivity, or enhanced mechanical properties. By adjusting the MOF's structure or incorporating it into hybrid composites, these materials can be engineered to deliver the mechanical strength, flexibility, and heat resistance required for advanced 3D printing applications. Furthermore, their high surface area and porosity offer the potential to create intricate, high-performance components suitable for diverse fields, including electronics, energy storage, and environmental remediation. Overall, the integration of thermally stable MOFs into 3D printing processes not only expands the range of materials available for fabrication but also unlocks new possibilities for creating functional, heat-resistant structures with enhanced performance.[84]

The thermal stability of MOFs can be substantially enhanced through precise structural design and dimensional engineering. For example, Guo *et al.*[85] developed the LCUH-101

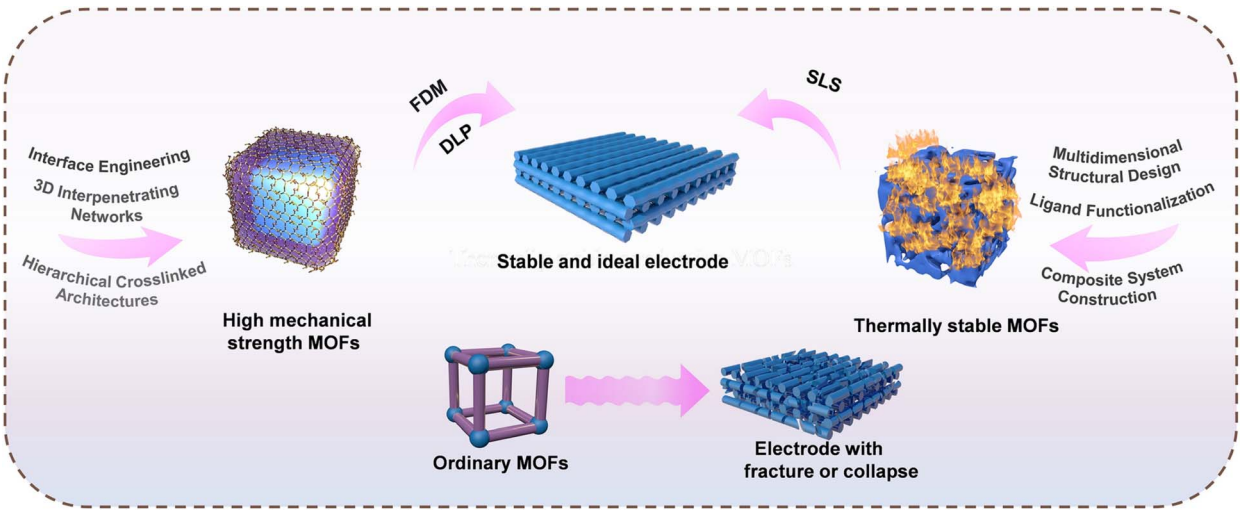

Fig. 5 Enhancing MOF-based electrode performance: the critical role of high mechanical strength MOFs, thermally stable MOFs, and multidimensional structural design in electrode fabrication *via* advanced 3D printing techniques.

series by strategically integrating anthracene chromophores and amino functionalities. The resulting 2D layers self-organize into a thermally robust 3D architecture *via* synergistic π–π stacking and hydrogen bonding—a dual stabilization mechanism that concurrently achieves three critical objectives: (1) maintaining structural integrity at >400 °C, (2) creating tunable interlayer galleries (4.97–6.95 Å) for molecular transport, and (3) spatially isolating catalytic Pd nanoparticles to mitigate sintering. This multidimensional approach establishes a design paradigm in which framework dimensionality directly dictates both stability and multifunctionality (Fig. 6a). Building on these 2D stabilization strategies while introducing chemical innovation, Tan *et al.*[86] reported a simple and mild liquid-phase synthesis route to rapidly produce a new lead-free high-energy MOF, $[Zn_2(atz)_3(N_3)]_n$, using the commercially available ligand (atz). The resulting nitrogen-rich Zn-MOF ($[Zn_2(atz)_3(N_3)]_n$) demonstrates exceptional thermal stability, with a decomposition temperature as high as 362 °C, far surpassing that of most previously reported MOFs, thus highlighting its outstanding heat resistance. Structurally, $[Zn_2(atz)_3(N_3)]_n$ features a unique graphene-like bilayer 2D framework bridged by azide groups. These two layers are interconnected through the coordination of Zn2+ ions with the azide linkers, which reinforces the overall rigidity of the MOF architecture. The azide "bridges" not only connect the bilayer structure but also safeguard the high-energy azide groups, substantially enhancing the stability of the entire MOF (Fig. 6b).

Transitioning from planar to chiral 3D architectures, Wang *et al.*[87] synthesized a ligand (H_3L) with strong coordination capabilities and a rigid framework, which was then combined with lanthanide metal ions Eu(III) and Tb(III). Using a solvothermal method, they successfully constructed a 3D helical MOF structure. The chiral ligand H_3L, which contains three carboxyl groups and one carbonyl group, forms stable coordination bonds with Ln3+ (lanthanide ions). This results in a homochiral helical framework composed of four intertwined helices (Fig. 6c). Collectively, these findings highlight that multi-dimensional structural design combined with robust coordination networks are effective strategies for improving the thermal stability of MOFs.

Ligand functionalization and chemical modification offer molecular-level solutions for enhancing the thermal stability of MOFs. Focusing on metal–ligand interplay, Chen *et al.*[88] investigated the thermal decomposition behaviors of four types of M-BTC (M = Cu, Co, Zn, Ce) under various atmospheres, including air, nitrogen, and hydrogen. The incorporation of Pt NPs was found to increase the ligand-to-metal charge transfer (LMCT) effect in Cu-BTC, which weakened the coordination between the metal center and the ligand, thereby reducing thermal stability. In contrast, for Ce-BTC, the introduction of Pt NPs had little impact on the LMCT effect, resulting in improved thermal stability. Under a hydrogen atmosphere, the carboxyl groups within the MOFs underwent hydrogenation, forming more stable structures and further enhancing thermal stability. Shifting focus to energetic MOF design, Zhang *et al.*[89] explored the thermal stability of high-energy MOFs based on 5,5′-azotetrazole-1,1′-diol (H_2AzTO) and their catalytic effect on the decomposition of ammonium perchlorate (AP). H_2AzTO, as a ligand, features an extensive π–π conjugated system and numerous hydrogen bond donor sites. Within the E-MOFs,

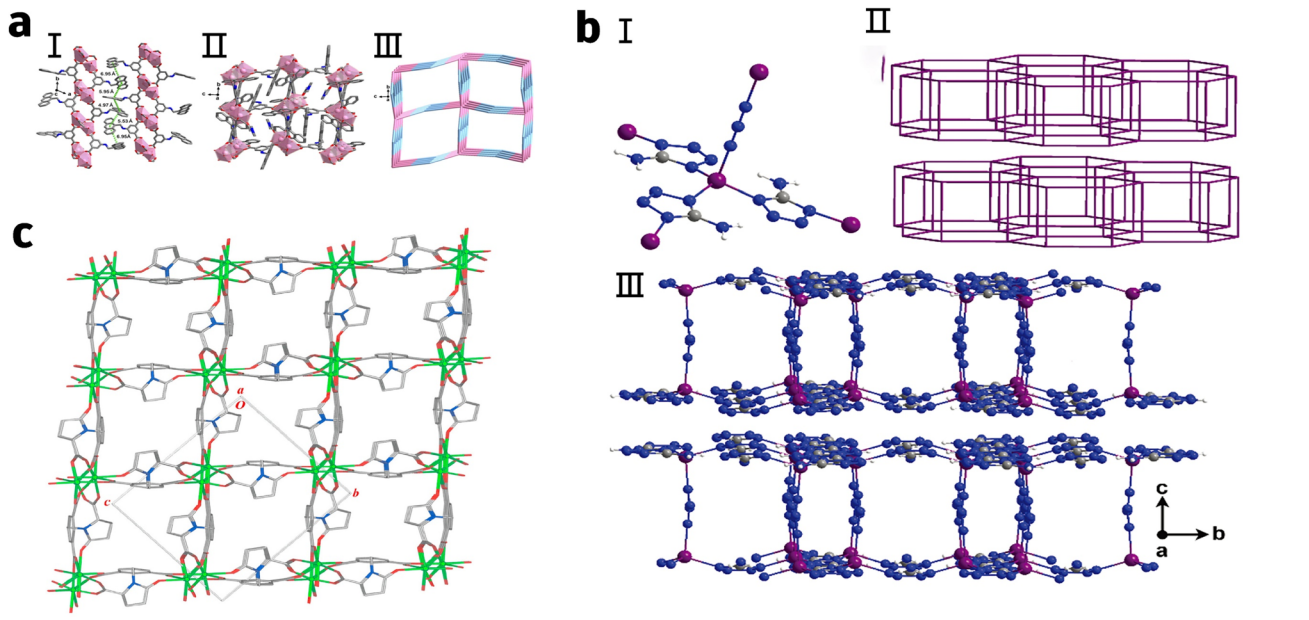

Fig. 6 (a) (I) Stratified architecture of the 2D framework oriented along the *c*-axis. (II) Mesh-like topology of the *a*-axis-aligned reticular system in europium-doped LCUH-101. (I) Streamlined topological schema of europium-integrated LCUH-101. (b) (I) Ligand coordination sphere of divalent zinc centers in the $[Zn_2(atz)_3(N_3)]_n$ matrix. (II) Dual-layer hexagonal topology mimicking 2D carbon allotropes. (III) Extended lattice architecture oriented parallel to the crystallographic *a*-axis. (c) Three-dimensional enantiopure framework exhibiting unidirectional channel alignment along the *a*-axis.

these hydrogen bonds create a robust network that reinforces both thermal and structural stability. The coordination between the metal ions and H_2AzTO ligands leads to the formation of a 3D framework that not only increases the material's density but also strengthens its stability through hydrogen bonding interactions (Fig. 7a). Pioneering post-synthetic stabilization strategies, Wang *et al.*[90] successfully synthesized a γ-CD-MOF with high thermal stability by employing an ethanol-mediated synthesis method and further enhanced its thermal stability through the incorporation of EGCG. The hydrophobic portion of EGCG interacts strongly with the hydrophobic cavities of γ-CD-MOF, stabilizing the encapsulated structure. Additionally, some EGCG molecules also interact with the aromatic rings of γ-CD-MOF through π–π stacking, significantly strengthening intermolecular binding and enhances thermal stability. Hydrogen bonds formed between EGCG and γ-CD-MOF further strengthen the intermolecular interactions, thereby improving the overall structural stability. Such strategies demonstrate how optimizing the chemical environment and interfacial interactions of MOFs through ligand–metal cooperation or post-synthetic modifications can effectively prevent structural collapse at high temperatures (Fig. 7b).

The construction of composite materials or the introduction of external support systems represents an innovative direction to addressing the thermal stability limitations of MOFs. Liang *et al.*[91] developed a MOF@MPCA composite material that effectively improves the thermal stability of MOFs. The carbon nanotube aerogel (MPCA), known for its inherent thermal resilience, significantly enhances the material's overall heat resistance when integrated with MOFs. During fabrication, chitosan and glutaraldehyde were employed to crosslink the MOF@PCMWCNTs, producing an aerogel with a distinct layered structure. This crosslinking not only reinforces the material's mechanical strength but also amplifies its thermal stability. At elevated temperatures, metal ions within the MOFs, such as Zn and Zr, form stable oxides (ZnO and ZrO_2) that resist decomposition, thereby providing additional thermal protection for the composite. Liu *et al.*[92] successfully fabricated a composite membrane with enhanced thermal stability by integrating UiO-66 with OPBI. The structural integrity of UiO-66 is maintained at high temperatures, offering a robust foundation for the membrane's thermal stability. OPBI, a polymer with excellent thermal resistance and inherent flame-retardant properties, further contributes to the composite's heat endurance. By combining UiO-66 with OPBI, the resulting membrane benefits from both the polymer's thermal stability and the MOF's porous structure. Prepared using a non-solvent-induced phase separation (NIPS) method, the membrane features a dual-channel architecture that enables efficient ion transport while its porous framework further boosting thermal stability. Li *et al.*[93] developed a multifunctional full name (ANF@MOFs) separator by *in situ* growing MOFs on a highly porous ANF network substrate. After heating at 200 °C for 0.5 hours, the ANF@MOFs composite separator maintains its dimensional stability, whereas traditional polypropylene (PP) separators begin to soften at 120 °C, shrank drastically at 180 °C, and nearly disappear at 200 °C. The MOF's high surface area (24.78 m2 g−1) and uniform pore size (∼30 nm) restrict polysulfide diffusion through physical adsorption. With high porosity (72.6%) and excellent electrolyte wettability (contact angle of 14.2°), the ANF@MOFs separator significantly improves lithium-ion conductivity, achieving three times the conductivity of the PP separator. These studies demonstrate the potential of multi-component synergistic effects to optimize thermal

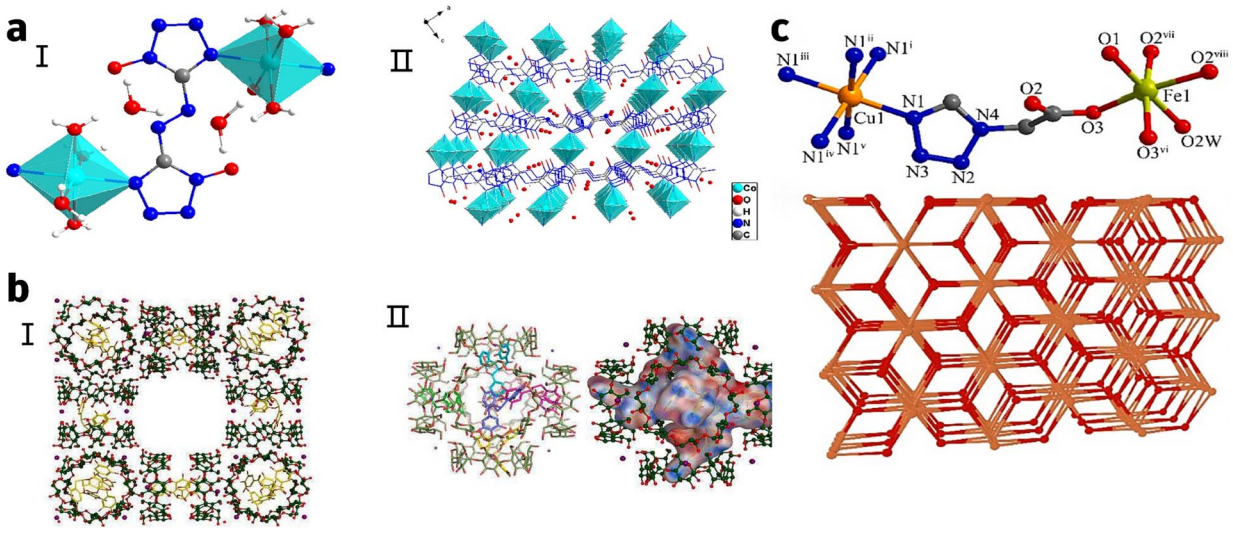

Fig. 7 (a) (I) Metal–ligand configuration of divalent cobalt centers within the crystalline lattice. (II) Stacked coordination polyhedra constituting the cobalt-centric 3D architecture. (b) (I) Hollow structural depiction of γ-CD-MOF-EGCG's supramolecular lattice, highlighting toroidal γ-CD units (green), EGCG ligands (yellow), and charge-balancing K+ ions (purple). (II) Atomic connectivity model of the hexameric γ-cyclodextrin assemblies, with γ-CD (green) and K+ (purple) spatial distribution. Complementary panels detail EGCG's molecular conformation (left) and electrostatic surface topography (right). (c) Cu2+ and Fe3+ coordination spheres within a cationic heterometallic lattice, with associated topological analysis of the CuFe-MOF.

stability, offering a new paradigm for the practical engineering applications of MOFs.

In addition to the above-mentioned methods, other strategies have been explored to enhance the thermal stability of MOFs. Using a straightforward and efficient method, Shi *et al.*[94] developed a 3D Cu–Fe high-energy MOF with enhanced thermal stability achieved through structural optimization. The CuFe-MOF exhibits remarkable thermal stability, with a thermal decomposition temperature of 238.9 °C. This MOF features an infinite 3D network composed of $[Fe_3O(tza)_6]$+ and Cu2+ ions. In the structure, Fe(III) ions adopt a distorted octahedral geometry, while Cu(II) ions coordinate with six nitrogen atoms to form an almost perfect octahedral configuration. The robust stability of this 3D framework significantly contributes to the overall thermal stability of the MOF (Fig. 7c). Gao *et al.*[95] developed a novel Ni MOF with a flower-like structure that exhibits excellent thermal stability. The unique flower-like arrangement arises from the assembly of petal-like layers, which likely form due to the exposure of different crystal planes. This structural design enhances stability at elevated temperatures while increasing the availability of active sites. Notably, the thermal stability of the Ni MOF lowers the dehydrogenation temperature of MgH_2 and significantly improves the kinetics of both hydrogenation and dehydrogenation processes.

2.3 Mechanical strength enhancement

Conductive MOFs exhibit high mechanical strength, enabling the development of dual-functional 3D printing materials that combine structural robustness with electrical conductivity for next-generation applications. The inherent mechanical robustness of these MOFs ensures that printed objects retain their structural integrity even under mechanical stress, while their conductive properties facilitate the fabrication of functional components for electronic devices, sensors, and energy storage systems.[96,97] Additionally, the tunable nature of MOFs allows for the incorporation of specific metal ions or organic linkers, which can be tailored to further enhance both conductivity and mechanical performance for targeted applications. By integrating conductive MOFs into 3D printing inks, it becomes possible to produce materials that are simultaneously mechanically resilient and electrically active, thereby expanding the range of printable applications in fields such as wearable electronics, smart devices, and energy-efficient technologies. With their high surface area, intrinsic porosity, and customizable structure, conductive MOFs are poised to play a pivotal role in shaping the future of advanced technologies of 3D printing.[98,99]

In recent years, strengthening the interfacial interactions between MOFs and polymer matrices has become an important strategy for improving the mechanical properties of composite membrane materials. Building on this principle, Satheesh Kumar and co-workers[100] achieved remarkable improvements in the structural robustness of hybrid membranes by leveraging the cooperative effects between MOF architectures and PBI polymeric networks, while utilizing the inherent porosity of MOFs to anchor proton-conductive species. The incorporation of MOF constituents effectively constrained segmental mobility within the PBI matrix *via* enhanced interfacial bonding, consequently augmenting the mechanical characteristics. This strengthening effect arose from the exceptional surface area and diverse functional moieties of MOFs, which facilitated robust molecular-level adhesion with PBI backbones, culminating in superior integrated mechanical performance of the membrane systems (Fig. 8a). Advancing beyond static architectures, Liu and collaborators[101] engineered ZIF-L(Co)-functionalized PMIA separators through *in situ* MOF growth. The innovation lies in the lamellar ZIF-L(Co) morphology, which not only amplified interfacial coupling with PMIA substrates but also exposes coordination-unsaturated sites that help Li+ flux homogenization. By preserving PMIA's intrinsic tensile modulus while incorporating MOF-derived stability, the Z-PMIA system overcame traditional strength degradation from weak heterointerfaces.

Transitioning from structural to electrochemical interfaces, Miao *et al.*[102] developed the AC-MCG gel interlayer, where MOF-polymer integration synergized with FEC additives. The hierarchical design leveraged the flexibility of polymers and the inherent rigidity of MOFs to balance fracture toughness with load-bearing capacity. Crucially, the formation of FEC-derived NaF passivation layers at the electrode interface improved mechanical integrity while suppressing dendrites growth—a dual-function strategy that bridges mechanical reinforcement and electrochemical stabilization. In another work, Lin *et al.*[103] achieved an unprecedented 89% MOF loading with CNC composites through hydrogen-bond networking. The breakthrough stems from CNC's dual role as both a mechanical reinforcer (*via* extensive H-bonding) and a MOF dispersant, which preserves proton conductivity while overcoming typical brittleness at high MOF content. This bioinspired synergy yielded membranes with unmatched mechanical strength and environmental stability (Fig. 8c). The synergistic integration of these two components has led to the creation of a versatile and robust membrane that holds great promise for various electrochemical and energy-related applications. While interfacial control strategies have proven effective for mechanical reinforcement, researchers are now overcoming the intrinsic mechanical limitations of MOF composite systems from the material topology level through structural design innovations. Recent innovations are transcending these approaches through topological redesign— marking a paradigm shift targeting MOF composites' intrinsic mechanical bottlenecks.

Structural engineering strategies provide a new dimension for improving the mechanical properties of MOF composites by constructing multi-level cross-linked networks or 3D interpenetrating topologies. Pioneering covalent crosslinking approaches, Wang *et al.*[104] engineered a solid polymer electrolyte by integrating MOFs with PEGDA and PETMP *via* thiol-ene click chemistry. This molecular templating approach created a hierarchically crosslinked topology, achieving record tensile strength (12.3 MPa) and Li+ conductivity (0.42 mS cm−1 at 25 °C) while suppressing Tg to 45 °C a triple triumph enabled by MOF-embedded ion highways (Fig. 8b). Advancing this crosslinking concept into 3D architectures, Cheng *et al.*[105] developed

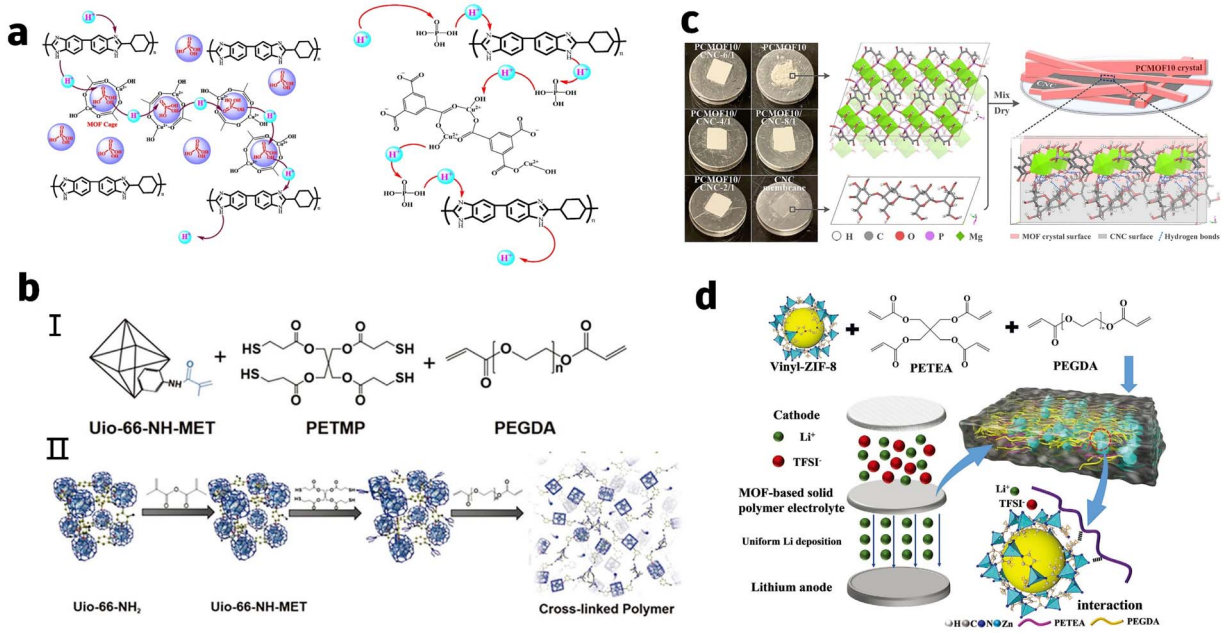

Fig. 8 (a) Mechanism of proton conduction in phosphoric acid doped composite membranes. (b) (I) Principal reagents for synthesizing interpenetrated polymeric matrices. (II) Assembly strategy and hierarchical representation of M-S-PDA, showcasing its composite architecture. Symbolic notation: cyan spheres (lithium ions), ultramarine blocks (porous MOF scaffolds), and deep-blue fibrils (PEGDA cross-linkers). (c) Schematic illustration showing the composite of PCMOF10 and CNCs. (d) (I) Main chemicals for the synthesis of cross-linked polymers. (II) Structure illustration of P-PETEA-MOF and illustration of conduction for lithium ions.

a MOF-808/PAN composite through electrospinning. The breakthrough lies in its 3D interconnected network, where MOF-induced polymer amorphization (crystallinity reduced by 38%) simultaneously enhanced ionic transport and mechanical robustness. By aligning structural reinforcement with dendrite suppression, this design extended battery cycle life by 2.7× compared to conventional electrolytes. Further extending the 3D network paradigm, Zhou *et al.*[106] successfully enhanced both the mechanical strength and ionic conductivity of polymer electrolytes by constructing a 3D cross-linked network based on MOFs. This design not only significantly suppressed lithium dendrite growth but also improved the safety and cycling stability of the battery. The incorporation of MOFs expanded the amorphous region of the polymer, thereby reducing crystallinity and boosting both ionic conductivity and mechanical properties. The composite architecture strengthened the mechanical performance and optimized the ion transport pathways through the porous structure of MOFs and the flexibility of the polymer (Fig. 8d).

Research breakthroughs in interface engineering and structural topology innovation have effectively addressed the long-standing challenge of balancing mechanical performance and multifunctionality in MOF composites. Interface optimization strategies including hydrogen-bond networks, coordination anchoring, and covalent crosslinking significantly enhance molecular-level interactions between MOFs and matrices, mitigating brittleness while maintaining high MOF loadings. Concurrently, topological innovations like 3D interpenetrating networks and hierarchical crosslinking architectures intrinsically improve mechanical strength and electrical/ionic conductivity by reducing crystallinity and constructing ion transport pathways. This dual "interface-structure" modulation strategy not only endows materials with exceptional stress resistance and electrochemical stability but also enables functional customization through MOFs' tunable porosity, offering novel solutions for flexible electronics, high-safety batteries, and smart sensors. Nevertheless, challenges remain in achieving uniform MOF dispersion at large-scale fabrication and ensuring long-term interfacial stability under cyclic stresses. Future research efforts should focus on dynamic adaptive interfaces, multi-scale biomimetic architectures, and environmentally sustainable composite systems to bridge the gap between laboratory breakthroughs and industrial applications. Ultimately, these efforts will pave the way for on-demand manufacturing of structurally and functionally integrated advanced materials.

3 Shaping MOFs into 3D-Printable precursor forms

MOFs with tunable structures are promising precursors for 3D printing. Additionally, post-processing of 3D printed structures plays a decisive role in the success of the printed monoliths, with major post-processing steps including phase conversion, coating, and thermal treatment. This paper provides an overview of representative precursor materials for 3D-printed MOFs and outlines their current development status, alongside key post-processing techniques. The aim is to provide guidance for advancing 3D printing strategies that leverage the unique properties of MOF materials.

3.1 3D printing precursors

3.1.1 MOF-based inks. Preparing MOF materials into ink is the most common method for uniformly integrating MOFs into a 3D printing matrix. MOF ink was first developed by Thakka *et al.*,[107] who mixed MOF-74(Ni) and UTSA-16(Co) with bentonite as a binder and PVA as a plasticizer to obtain an ink that could be directly extruded. The commonly used DIW 3D printing method requires that MOFs be formulated into a suitable ink prior to printing. DIW is an 3D printing technique in which pre-prepared ink is extruded and layered to form a 3D object. A typical DIW process involves four steps: shape design, ink preparation, printing, and post-processing, with ink preparation being the most critical step. The rheological properties of the ink directly determine the success of the printing. An ideal 3D printing ink should exhibit high viscosity at low shear rates and low viscosity at high shear rates, ensuring that the ink does not flow out of the nozzle when stationary and extrudes smoothly during printing, forming a stable structure. Additionally, the mechanical properties and final morphology of the printed material are closely related to this process.

For DIW-compatible inks, it is crucial that MOF powders are in the micron size range or smaller to prevent nozzle clogging during extrusion. Additionally, a uniform particle distribution ensures good ink flowability and printing accuracy. DIW inks require high viscosity to maintain the shape of the extruded structures and prevent collapse during printing. To achieve this, MOF particles are typically blended with a high-viscosity polymer matrix or binder, producing a paste-like ink with suitable rheological properties. This matrix not only be compatible with the MOF materials but must also not compromise the structure and functionality during subsequent curing processes. Cellulose nanofibers, owing to their controllable rheological properties, provide a simple means of adjusting ink rheology. Bentonite, with its strong water absorption, swelling properties, and gel-like behavior in water, effectively binds MOF structures and enhances plasticity, making it a widely used additive in DIW ink formulations. Lefevere *et al.*[108] successfully developed

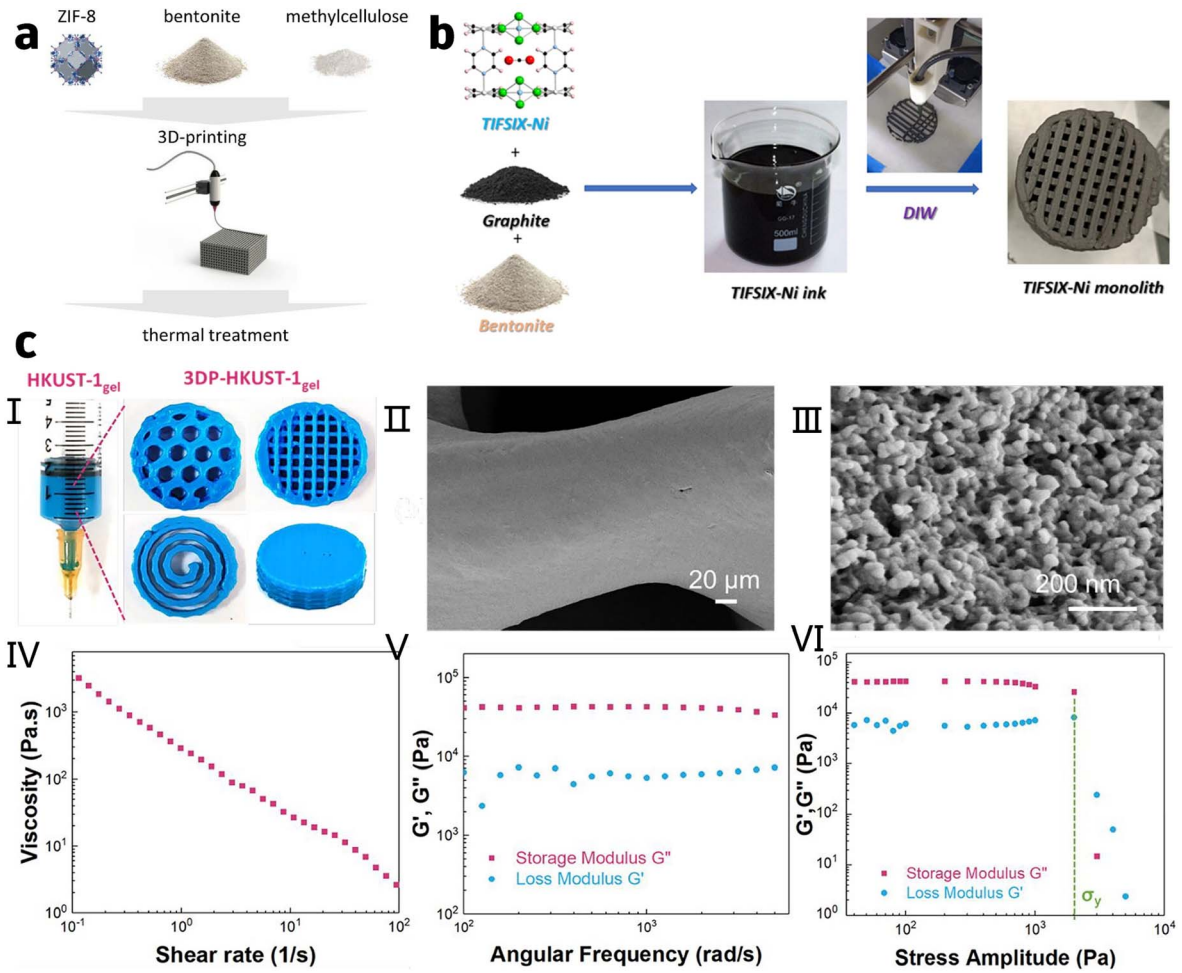

Fig. 9 (a) Graphical workflow of the synthetic protocol. (b) Robocast fabrication of a structurally engineered TIFSIX-Ni coordination polymer monolith. (c) (I) Syringe-loaded copper-based MOF hydrogel (HKUST-1) and derived 3D-printed geometries. (II) Microstructural analysis of a single filament in the desiccated 3D-printed HKUST-1 monolith. (III) High-resolution SEM visualization of HKUST-1 nanoparticles within the printed MOF-polymer composite. (IV–VI) Rheological properties: Static viscoelasticity (IV), dynamic shear-thinning (V), and pseudoplastic flow behavior (VI).

a 3D printing ink for n-butanol recovery by combining ZIF-8 with methylcellulose and bentonite as binders. The research team also devised an activation protocol using an inert (argon) atmosphere to remove the binder post-3D printing without damaging the ZIF-8 structure (Fig. 9a). In another study, Grande *et al.*[109] developed a non-aqueous cellulose ink by regulating its rheology with hydroxypropyl cellulose and boehmite, combined it with UTSA-16, this formulation was used to 3D print monoliths with excellent adsorption properties *via* the DIW technique. Kearns *et al.*[110] also mixed bentonite and carbon black with the hybrid ultraporous material TiF_6–Ni ($[Ni(pyrazine)_2(TiF_6)]_n$) to produce composite ink, achieving the first application of TIFSIX-Ni as a CO_2 capture agent through DIW.

Binder-free inks have also demonstrated promising applications. Compared to binder-containing inks, binder-free formulations simplify the binder removal step and allow for more precise control over ink viscosity. Additionally, the absence of binders improves the mechanical properties of the printed monoliths (Fig. 9b). Lim *et al.*[111] prepared HKUST-1gel and HKUST-1gel-TEA by separately dissolving organic ligands and metal compounds in organic solvents, followed by vigorous mixing. The resulting gels exhibited favorable rheological properties. To achieve high mechanical strength in printed objects, inks must have a high solid content. Increased solid loading improves the density and durability of printed structures, enabling them to withstand higher mechanical stress. Moreover, high solid content reduces material shrinkage and deformation, thereby improving printing accuracy and surface quality (Fig. 9c). Salazar-Aguilar *et al.*[62] prepared a water-based ink containing up to 64 wt% solid content by mixing an iron-based MOF with silicon carbide (SiC). They found that the high solid content provided good mechanical strength, with SiC's excellent rheological properties also contributing to further reinforcement. Subsequently, Salazar-Aguilar *et al.*[60] developed a new method by combining a pseudo-plastic iron MOF (Fe-MOF) with aqueous boehmite to prepare an ink, successfully printing a 3D cellular Fe/γ-Al_2O_3 monolith with a total porosity of 88% and low density (0.43 g cm−3). Compared to the previously used SiC, the γ-Al_2O_3 offered a higher specific surface area, lower cost, and better corrosion resistance and mechanical properties. Hussain *et al.*[112] prepared an ink for photocatalytic applications by mixing Ti-MOF NH_2-MIL-125 with a boehmite dispersant, demonstrating that the hydrogen evolution performance of the 3D-printed Ti-MOF-derived monoliths was five times higher than that of the same photocatalyst in powder form.

The development of MOF-based EES devices using DIW is still in its early stages, but initial explorations have shown promising potential. Lyu *et al.*[61] successfully prepared 3D-printed monoliths with excellent conductivity and mechanical stability by formulating ink from Co-MOF and Pluronic F127 powder dissolved in cold water at 4 °C. The 3D structure was preserved after annealing in an N_2 atmosphere (Fig. 10a). Xi *et al.*[113] prepared an Al-MOF/S ink by mixing Al-MOF/S powder, conductive carbon black, and polyvinylidene fluoride (PVDF) in a mass ratio of 7 : 2 : 1, grinding the mixture in a mortar for 10 minutes. *N*-methyl-2-pyrrolidone (NMP) solution was then added dropwise and thoroughly mixed to obtain an ink with desirable rheological properties (Fig. 10b). A significant and groundbreaking study was conducted by Zhou *et al.*,[114] who uniformly grew ZIF-67 on V_2O_5NWs and then performed Co2+ and Ni2+ ion exchange in ethanol solvent, resulting in spatially separated active sites on the surface (Fig. 10c). They developed a 3D-printed micro-supercapacitor (MSC) with higher capacitance, energy density, and a broader voltage window by mixing the MOF with graphene oxide (GO) and carbon nanotubes

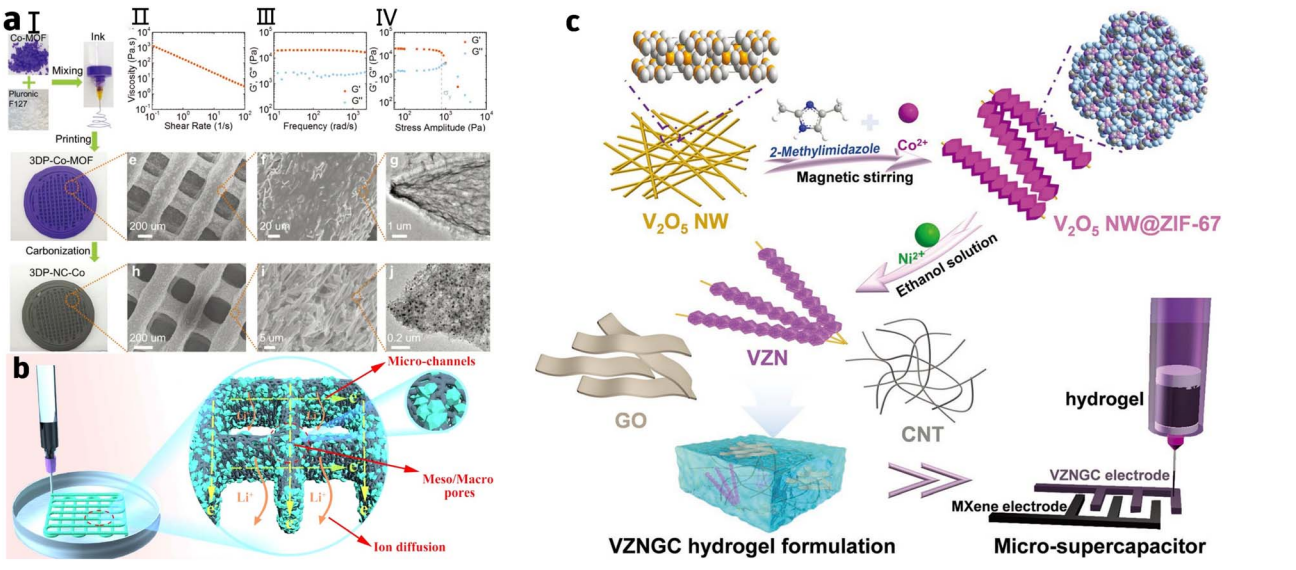

Fig. 10 (a) (I)Assembly protocol for the robocast Co-MOF hierarchical structure. (II–IV) Rheological analysis of the CoMOF-F127 ink: Gel-phase rigidity at rest (II), viscosity reduction under shear stress (III), and pseudoplastic flow profile (IV). (b) Redox species conduction model for the robocast Al-MOF-160/S electrode architecture. (c) (I) Illustrative diagram outlining the synthesis process of VZN. (II) Schematic representation detailing the architecture of the 3D-printed micro-supercapacitor.

(CNTs) to produce an ink. Subsequently, Zhou *et al.*[74] further advanced this research by stabilizing Ni, which has a stronger coordination ability, in nano-Co-MOF, and subsequently mixed it with GO and CNTs to prepare an ink suitable for DIW. This enabled the production of high-resolution interdigitated electrodes for 3D-printed MSCs. The resulting electrodes exhibited excellent electrochemical performance, paving the way for the development of MOF-based 3D-printed electrodes.

3.1.2 Composite filaments. FDM operates by extruding thermoplastic polymers heated beyond their glass transition temperature (typically 180–220 °C) to build objects layer-by-layer. Incorporating conductive fillers such as CNTs or graphene enables the fabrication of electrically functional structures. At the nozzle, the polymer melt undergoes rapid phase transition to solidification (cooling rate > 50 °C s−1). The thermoplastic nature of the material allows for effective bonding and solidification at room temperature. The mechanical properties depend on multiple factors, including filament dimensions, orientation, inter-layer gaps, and distortions. Combining thermoplastics with active materials enhances filament properties. Common feedstocks include polylactic acid (PLA), polycaprolactone (PCL), and acrylonitrile butadiene styrene (ABS), valued for their processability, biodegradability, and versatility. In advanced FDM applications, thermoplastic filaments can be combined with electrically conductive composite filaments within a single print process.[115–117] This combination allows for the creation of structural electronics, wherein electrical circuits, sensors, and other components are seamlessly embedded within the printed polymer structures. Such integration is paving the way for innovative applications in fields like wearable technology and smart devices, where merging mechanical and electronic functionalities within a single part is highly desirable. The ability to fabricate these multifunctional structures through a layer-by-layer process is opening up new possibilities for customized and complex designs, potentially revolutionizing how electronic devices are manufactured and utilized.[118,119]

The technology for converting MOF materials into FDM filaments remains in its nascent stages. While initial research has shown promising feasibility, there are significant challenges to overcome, including the need to optimize fabrication processes, improve material properties, and ensure compatibility with existing 3D printing technologies. Continued advancements in this area are essential to fully unlock the potential of MOFs for 3D printing applications. Kreider *et al.*[120] successfully fabricated MOF monoliths capable of hydrogen absorption by incorporating MOF-5 into an ABS matrix. Their results demonstrated that the composite could be reliably printed as long as the MOF-5 content remained below 10%. It is particularly noteworthy that, owing to the interactions between the polymer and the MOF, the polymer's other physical and mechanical properties, including glass transition temperature, stress and strain at the break point, and Young's modulus, either remained unchanged or showed a certain degree of hardenings. Building on thermoplastic processing, Wu *et al.*[121] developed a multi-stage derivatization strategy: ZIF-67 was first grown on carbon fibers (CF), followed by melamine annealing and CNT modification to produce CoNC@CF (Fig. 11a). This derivative was then blended with a PLA solution and extruded into FDM-printable CoNC@CF-PLA filaments (Fig. 11b), effectively circumventing structural collapse during thermal processing through MOF derivatization. In parallel, PCL has emerged as an ideal substrate for thermally sensitive MOFs due to its low melting point (60 °C). Its mild processing conditions maximizes MOF pore structure retention, opening new avenues for high-loading filaments with framework integrity. These studies systematically advance the field of MOF-functionalized filaments along three parallel pathways: direct blending, derivative conversion, and low-temperature processing. However, critical technical barriers – including interfacial compatibility and melt rheology control – must be overcome to achieve high-MOF-content (>30%) printable systems.

Furthermore, the mechanical properties of PCL, such as strength and rigidity, can be effectively enhanced by incorporating additional fillers like carbon fibers, making it a versatile material for diverse applications. Oh and colleagues[122] developed two types of polymer filaments by compounding PLA with either FI-MOF or FI-ph-MOF. Their findings confirmed that the Fl-ph-MOF@PCL filament exhibits both fluorescence and room-temperature phosphorescence (RT-OP), demonstrating its multifunctional nature (Fig. 12a). In contrast, the Fl-MOF@PCL filament displayed only fluorescence under UV light and did not exhibit RT-OP, highlighting the distinct photophysical properties of the two filaments (Fig. 12b). Additionally, in recent years, the environmentally friendly and biodegradable material PLA has also attracted widespread attention as a polymer matrix for MOF composites. Simões and his team [123] successfully prepared a uniform PLA/LnMOF composite by incorporating freshly synthesized europium (EuMOF) and terbium (TbMOF) LnMOFs into the PLA polymer (Fig. 12c). This was achieved through a two-step process involving solvent casting followed by melt blending, which ensured homogeneous dispersion of the LnMOFs within the PLA matrix. The resulting composite was subsequently processed using a filament extruder to produce high-quality filaments specifically designed for 3D printing applications, such as QR codes.

FDM technology shows considerable potential for compatibility with a wide range of polymer substrates, making it a promising approach for fabricating MOF monoliths. Nevertheless, a key limitation in applying FDM to 3D printing MOF-based electrochemical devices lies in the insufficient electrical conductivity of the polymer substrates and the limited thermal stability of MOF materials. These challenges indicate the need for continued research to identify MOFs with higher thermal stability and better electrical conductivity. Additionally, there is a pressing demand for the development of highly conductive polymer substrates that can be easily integrated with MOFs to form stable and efficient composites. Such advancements could significantly enhance the viability of using FDM to fabricate next-generation MOF-based electrochemical devices.

3.1.3 Photosensitive resins. Technologies that enable the incorporation of MOFs into liquid photosensitive resins for advanced 3D printing applications include DLP, SLA, and Two-Photon Polymerization (TPP). These methods offer distinct

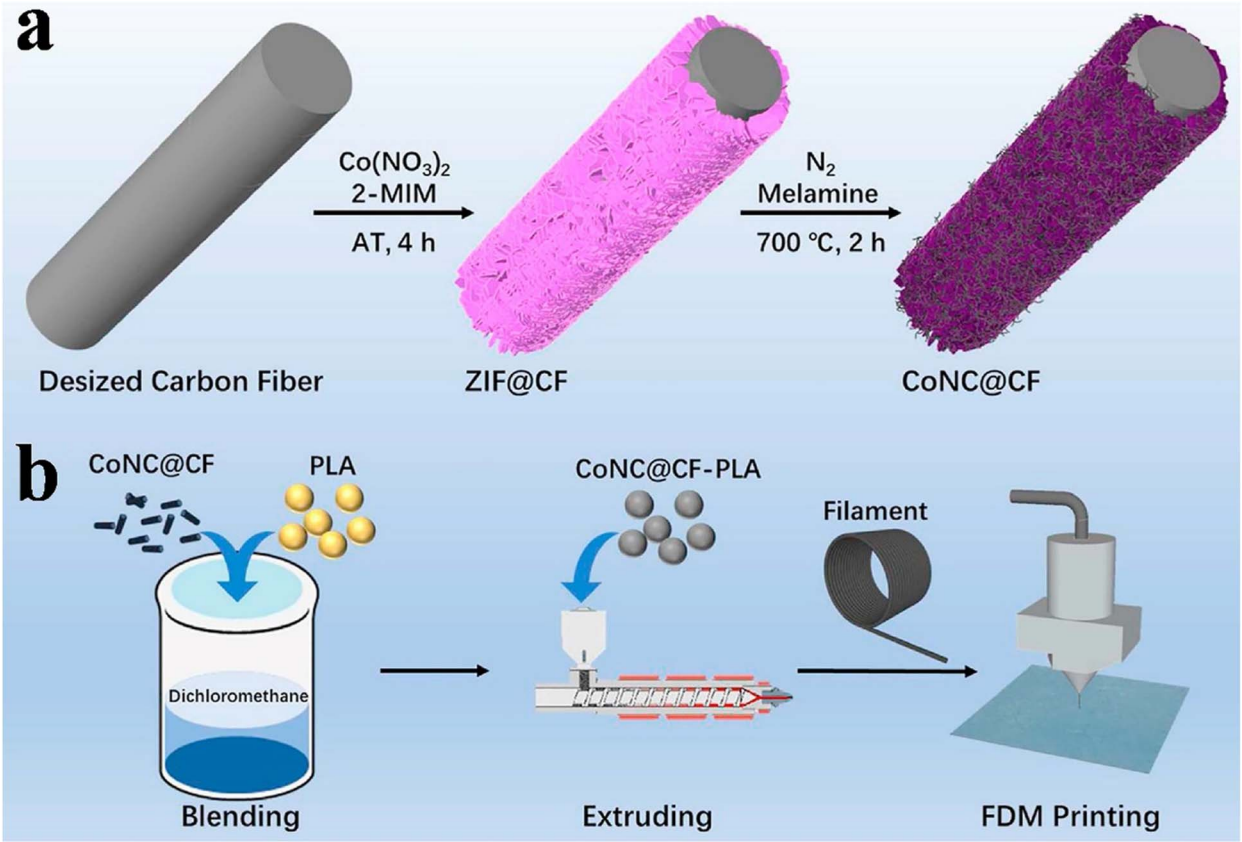

Fig. 11 (a) Flowchart depicting the synthesis of CoNC@CF, and (b) schematic overview of fabricating CoNC@CF-PLA nanocomposite filaments followed by their processing *via* FDM printing.

advantages such as high resolution, efficient material utilization, and the ability to create intricate geometries, making them particularly well-suited for fabricating complex MOF-based structures with enhanced functionality. Grouped under the broader category of photopolymerization methods, these technologiesoperate on the essential principle of light-driven polymerization. In this process, a fluid light-sensitive polymer undergoes a polymerization transformation upon being illuminated by a light source. As a result, the resin progressively solidifies layer by layer, ultimately forming a 3D configuration precisely defined by computer-aided design frameworks.

Photopolymerization printing enables precise manipulation of the morphology of MOFs and supports the efficient and rapid fabrication of MOF monoliths. Nevertheless, several inherent limitations remain when applying photopolymerization techniques to printing MOF monoliths. The primary challenge is the selection of appropriate materials; the resin must not only preserve the porous structure of the MOF but also be compatible with the photopolymerization process to ensure successful fabrication. Acrylic resin are often preferred due to their rapid curing, high resolution, tunable material properties, excellent transparency, and strong chemical resistance, making them ideal candidates for liquid photopolymer resin. Halevi and colleagues[55] were the first to successfully fabricate complex 3D structures embedded with MOFs. They dispersed Cu-BTC into 2-phenoxyethyl acrylate (Sartomer SR-339), where the monoaromatic group in this monomer significantly enhanced its affinity for the MOF particles, resulting in a stable dispersion without the need for any additional dispersing agents. Furthermore, the hydrophobic properties of the monomer enhanced the hydrolytic stability of the embedded MOF. To reinforce the structural stability of the polymer matrix, polyethylene glycol (600) diacrylate (SR-610) – a bifunctional acrylate crosslinker – was incorporated into the system. Simultaneously, a dual-photoinitiator strategy comprising Irgacure-819 and Irgacure-184 was implemented to optimize the photopolymerization kinetics and ensure process reliability. The resulting liquid photosensitive resin enabled the successful fabrication of a flexible 3D object with embedded MOFs.

Building on these material innovations, Pustovarenko *et al.*[124] achieved covalent integration of methacrylate-functionalized MIL-53(Al)–NH_2 nanoparticles into an acrylic oligomer matrix using Irgacure 819 as a photoinitiator. DLP technology, they successfully fabricated photopatterned MOF composite membranes with a 12 wt% MOF loading. The resin formulation combined ethoxylated-4-dihydroxyphenyl-2-propenoate, UDMA, TMPTMA, and amine-modified polyether acrylate, which together accelerated photo-crosslinking kinetics while ensuring dimensional stability. This work highlighted the importance of tailored monomer-MOF interactions in achieving high-performance composites without compromising process efficiency. Further expanding the functional applications of

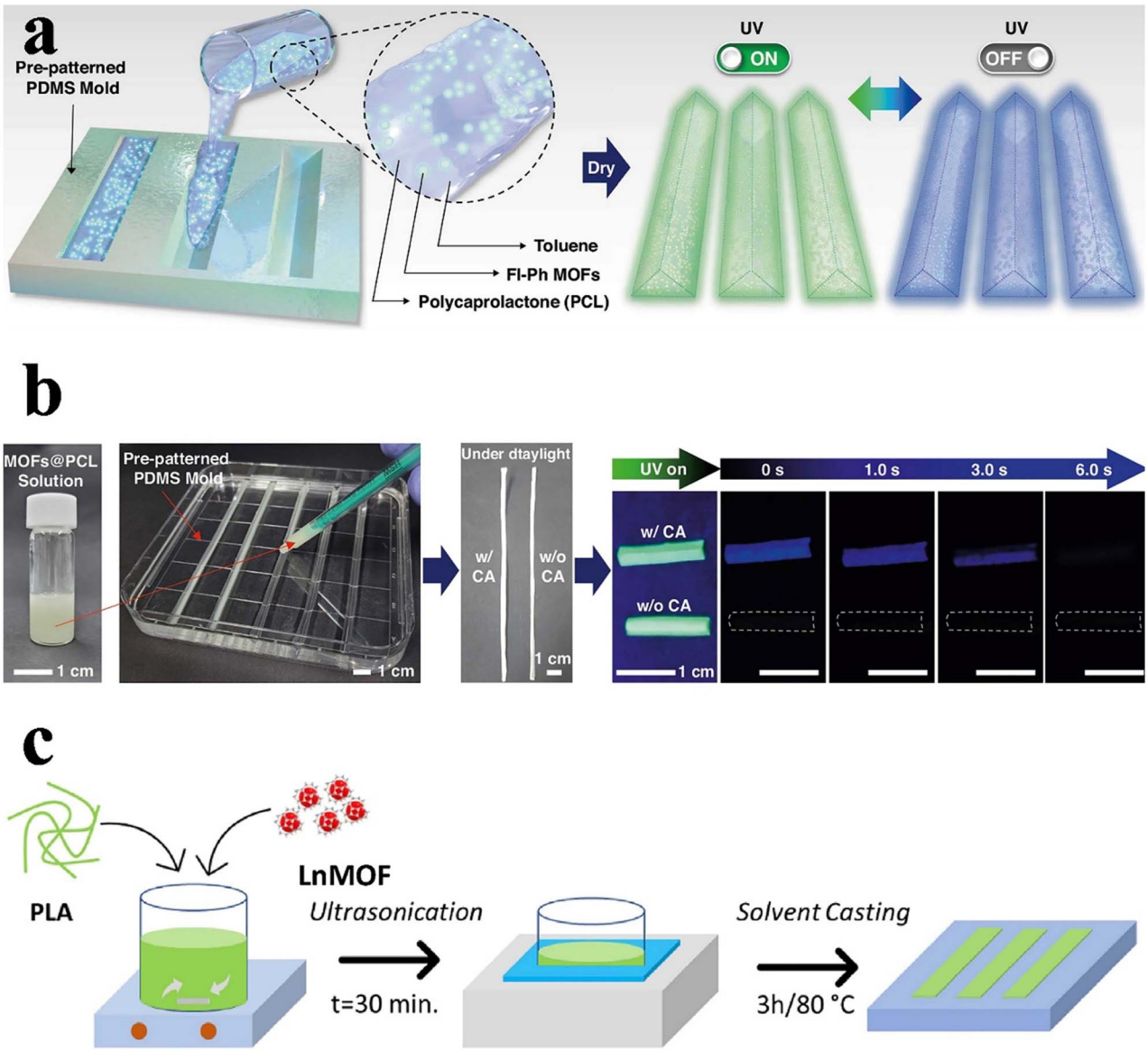

Fig. 12 (a) Diagram illustrating the fabrication process of PCL filaments embedded with Fl MOF and Fl–Ph MOF particles, produced using a pre-patterned PDMS mold. (b) Images capturing the stepwise fabrication of Fl–Ph MOF@PCL filaments, demonstrating the retention of dual luminescent properties throughout the process. (c) Diagram illustrating the processing workflow for PLA/LnMOF composite materials.

photopolymerized MOFs, Huong *et al.*[125] synthesized WO_3-UiO-66@rGO composite materials by combining WO_3-UiO-66 with GO *via* a solvothermal method. The resulting powder, prepared with 5% or 10% MOF loading, was uniformly dispersed in acrylic resin to fabricate 3D-printed catalysts using DLP technology. The photocatalytic degradation of (SMX) was evaluated under UV irradiation, with performance assessments demonstrating that the 3D-WO_3-UiO-66@rGO catalyst showed a markedly improved SMX degradation efficiency.

In addition to the careful selection of polymer substrates and nanomaterials, the cross-linking agent is also an important component of the photosensitive resin. Its primary function is to establish a network structure within the resin, thereby improving the mechanical strength, dimensional stability, and overall durability of the cured material. Perera *et al.*[126] utilized 2-hydroxyethyl acrylate (2-HEA) and 2-phenoxyethyl acrylate as the main polymer bases in their formulation. Tetraethylene glycol diacrylate (TEGDA) was added as the cross-linking agent, contributing 5 wt% to the overall resin composition. In addition, bis(2,4,6-trimethylbenzoyl)-phenylphosphine oxide served as the photoinitiator to generate catalytically active polymer monomers under relatively low MOF loadings. This approach not only preserved the mechanical integrity of the polymer but also retained the high-resolution advantages inherent to reduction-induced photopolymerization. In the field of biomedicine, methacrylated gelatin (GelMA) can also be applied as a photosensitive resin substrate. Choi *et al.*[127] developed osteoconductive hydrogel scaffolds by incorporating ZIF-8 into GelMA. Using lithium phenyl-2,4,6-trimethylbenzoylphosphinate as a visible-light-responsive

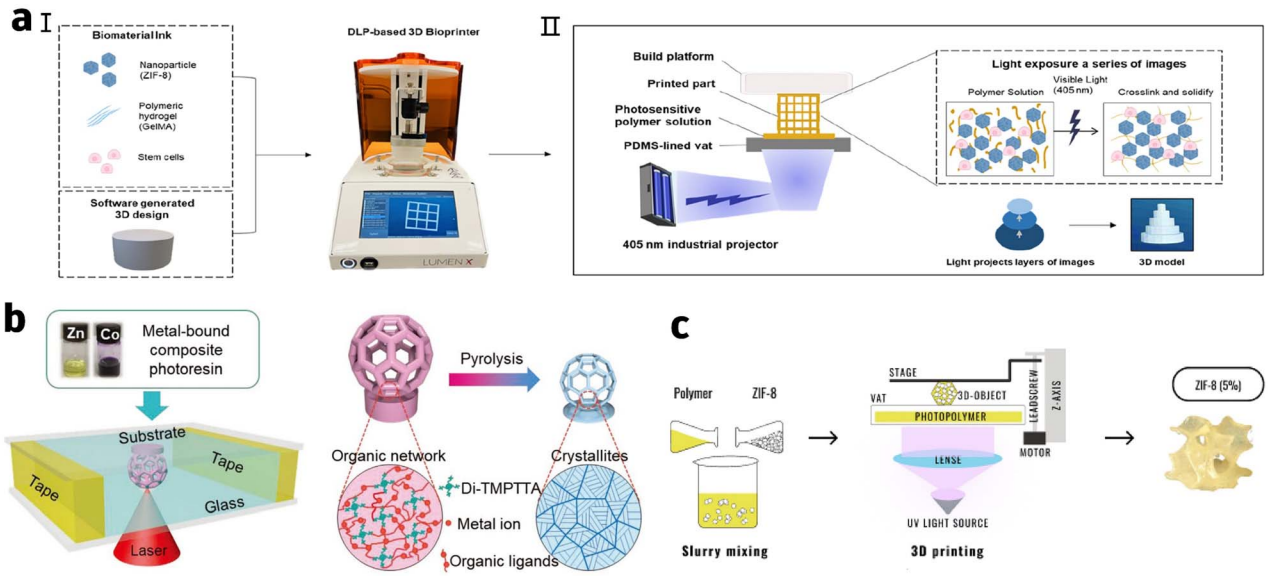

Fig. 13 (a) (I) Schematic diagram outlining the strategy used to fabricate 3D structures *via* a DLP-based 3D bio-printer. (II) Graphic illustrating the underlying principle of DLP-based 3D bio-printing technology. (b) The composite photoresin, containing metal, is patterned into three-dimensional nanostructures using TPP lithography. Subsequently, the fabricated 3D polymer framework is pyrolyzed in an oxygen atmosphere at 550 °C, yielding a corresponding 3D nano-architected metal oxide. (c) Strategy for 3D-printed porous ZIF-8.

initiator under 405 nm irradiation, they achieved precise zwitterionic coordination-mediated crosslinking. The resulting GelMA/ZIF-8 nanocomposite hydrogels exhibited spatiotemporal resolution and a bone-mimetic compressive modulus (18.7 ± 1.5 kPa), making them promising candidates for minimally invasive repair of trabecular defects (Fig. 13a). This work underscores the versatility of photopolymerization in tailoring MOF-polymer hybrids for advanced structural and biomedical applications.

Both TPP and SLA rely on light irradiation to initiate the polymerization of photosensitive resins, transforming liquid resin into solid structures. TPP employs a high-intensity laser beam to drive polymerization through nonlinear effects, enabling the fabrication of features with extremely small dimensions and outstanding precision. Given the stringent accuracy requirements of TPP, it is essential to formulate specialized resins that meet the high accuracy standards of the process. Liu *et al.*[128] combined MOFs with di(trimethylolpropane) tetraacrylate (Ditmptta) and acrylic acid to develop a hybrid polymer resin. Utilizing benzil as the photoinitiator and BDMP as the photosensitizer, they implemented TPP lithography followed by pyrolysis to produce ZnO and Co_3O_4 composite nanostructures exhibiting high spatial resolution, outstanding shape fidelity, and excellent surface quality. SLA employs a laser beam to scan the photosensitive resin dot by dot, selectively solidifying the specified regions. Because of the requirement for point-by-point scanning and curing, the process is comparatively slow. Therefore, the resin must respond rapidly to laser exposure and cure promptly at the designated wavelengths (Fig. 13b). Furthermore, the viscosity should be balanced to facilitate uniform application and swift curing during point-by-point scanning. Cherevko *et al.*[129] prepared a liquid photosensitive resin by blending 2-phenoxyethyl acrylate and trimethylolpropane triacrylate with di(2,4,6-trimethylbenzoyl)phosphine oxide and 1-hydroxycyclohexyl phenyl ketone in a PP cup. ZIF-8 and Ni-BTC were added to the resulting resin at a concentration of 5 wt%. Using SLA 3D printing and high-temperature pyrolysis, they produced novel porous carbon materials with embedded metallic particles, resulting in enhanced functionalities (Fig. 13c). Representative technologies such as DLP, SLA, and TPP enable efficient integration of MOFs with polymer matrices *via* light-controlled polymerization. Notable examples include Halevi's Cu-BTC/acrylate system and Pustovarenko's covalently grafted MIL-53(Al) membrane, highlight the critical role of optimized monomer-MOF interfacial interactions in the design photosensitive resins. Innovations in material systems extend beyond substrate selection (*e.g.*, high transparency of acrylic resins and biocompatibility of GelMA) to the synergistic design of crosslinkers, photoinitiators, and nanofillers. For instance, TEGDA enhances network stability, while dual-photoinitiator strategies improve curing efficiency. However, challenges persist: the intrinsic porosity of MOFs remains susceptible to polymer infiltration, the trade-off between uniform particle dispersion and increased light scattering at high loadings is yet to be fully resolved, and balancing high print resolution with mechanical properties continues to require further optimization. Future research should focus on multi-scale structure–function integration, as exemplified by Huong's 3D-printed photocatalysts and Choi's biomedical scaffolds, which demonstrate the cross-disciplinary potential of these systems in environmental and medical applications. By refining MOF surface functionalization and optimizing resin formulation synergy, it will be possible to realize advanced composites with high precision, preserved porosity, and tailored functionalities.

3.1.4 Sinterable powders. The preparation of materials in powder form for molding is predominantly applied in SLS

technology. At present, SLS printing is primarily used for polymers and metals, while the integration of MOFs, a novel class of porous materials, have not yet been fully integrated with SLS technology. Identifying suitable MOFs or their composites that can simultaneously satisfy the demands of SLS processing while retaining the functional properties of MOFs is still an early-stage research field. Nonetheless, the potential advantages of utilizing SLS for shaping MOFs are gaining increasing attention from researchers. In the SLS process, transient laser heating is employed to rapidly sinter or melt powder particles, resulting in the formation of pores. When MOF fillers are combined with polymer particles, these pores generate open pathways within the polymer matrix, thereby increasing the interfacial contact area between the fillers and the external environment. By fine-tuning key laser sintering parameters, such as laser power, scan speed, and hatch spacing, the quantity and size of these pores can be precisely controlled. Furthermore, SLS technology offers distinct advantages over other large-scale manufacturing techniques, such as electrospinning and hot pressing, particularly in fabricating multilayer structures with well-defined surface patterns. Utilizing advanced 3D powder-based printing, specifically SLS, Feng and colleagues[130] successfully fabricated MOF-polymer composite membranes. They used thermoplastic polyamide 12 powder as the base material and incorporated ZIF-67, NH_2-MIL-101(Al), MOF-801, HKUST-1, and ZIF-8 crystals as functional additives.

3.2 Post-processing & functionalization

3.2.1 *In Situ* transformation & hierarchical activation. *In situ* growth is an important technique for the preparation of MOFs monoliths. By incorporating various metal oxides or MOF precursors (*e.g.*, metal salts and organic ligands) into 3D-printed substrates as nucleation sites, it is possible to synthesize MOFs on already shape-defined materials. Thus, monomers can be generated through secondary growth using chemical precursors and templates, followed by the preparation of chemically active samples through *in situ* growth.[131–133]

The overall material printed using polymer filaments in FDM printing technology exhibits higher mechanical strength, which facilitates the *in situ* growth of MOFs. Additionally, polymer frameworks fabricated from widely available materials like PLA and ABS offer a more cost-effective alternative.[134] In this process, the filaments are recyclable, further reducing production costs and enhancing sustainability. These advantages make polymer frameworks printed with filaments a preferred choice for *in situ* growth applications. Wang[135] and colleagues successfully functionalized an ABS scaffold by coating it with the porous MOF, Cu-BTC (BTC – benzene-1,3,5-tricarboxylate), using a stepwise *in situ* growth technique. The resulting Cu-BTC/ABS composite demonstrated high Cu-BTC coverage, substantial adsorption capacity and efficient removal of methylene blue (MB) from water solutions. This study suggested that Cu-BTC/ABS composites could function as efficient adsorbents for environmental remediation, while also highlighting 3D printing as a rapid and sustainable approach for fabricating novel functional composites with applications extending beyond adsorption (Fig. 14a). Building on this concept, Shi[136] *et al.* substituted ABS filaments with PLA filaments and employed the same sequential *in situ* growth method to produce Cu-MOFs/PLA filaments. The Cu-MOFs/PLA membrane exhibited adsorption times exceeding 10 minutes across different concentrations, with removal efficiencies above 90%. Similar to ABS, PLA filaments are recyclable and reusable. Both methods involve the *in situ* growth of MOF materials on the polymer surface, which limits MOF loading within the material's interior.

Subsequent research has advanced the strategy by directly mixing MOF precursors with the polymer framework prior to

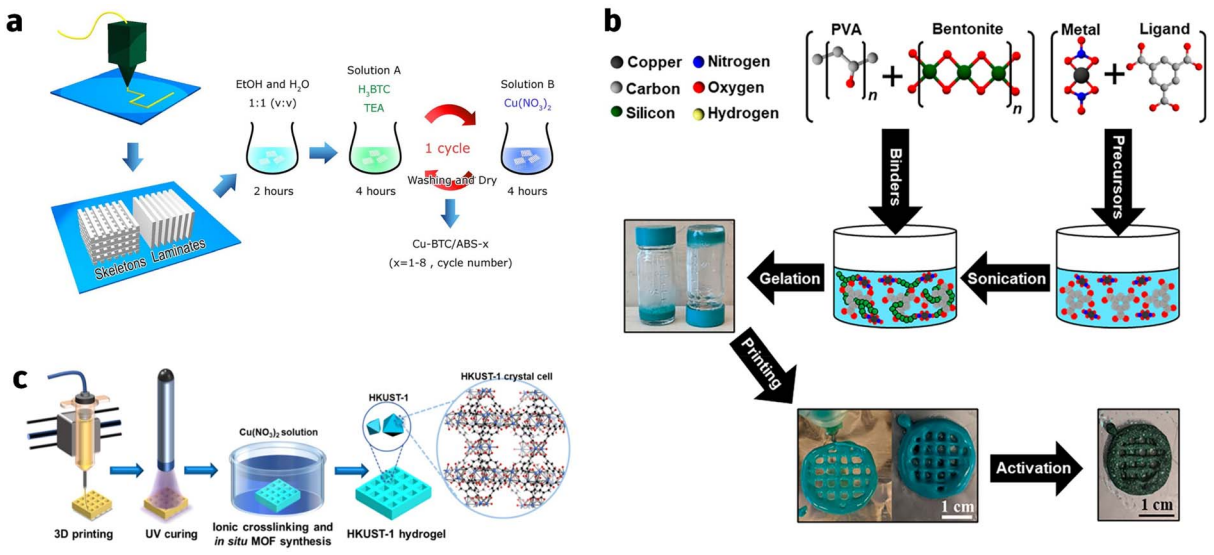

Fig. 14 (a) Preparation of composite materials integrating Cu-BTC with ABS. (b) Stepwise fabrication mechanism of HKUST-1 monoliths through the novel GPG strategy. (c) Visual protocol for the 3D bioprinting cascade: sequential deposition, UV-triggered solidification, and electrolyte-mediated crosslinking.

printing, thereby enabling MOF growth within the material's interior. Waheed[137] and colleagues developed composite filaments for fused deposition modeling that integrate active ZnO nanoparticles within a thermoplastic matrix. In these filaments, 10 wt% ZnO-NPs were uniformly distributed throughout an ABS matrix. When used for 3D printing, the resulting components served as substrates for the direct growth of ZIF-8 crystals. Under ambient conditions, a gentle chemical transformation converted the embedded ZnO nanoparticles into ZIF-8 crystals, which formed on the surfaces of the printed parts. The authors compared this method with the direct incorporation of pre-synthesized MOFs into the 3D printing equipment. The *in situ* growth technique enables crystal formation after printing, effectively avoiding the issue of MOF crystals becoming encapsulated within the polymer and inaccessible for functional applications. However, this method typically achieves relatively low MOF loadings due to constraints on precursor content and conversion efficiency. To address this limitation Lawson[138] *et al.* developed a new approach by utilizing 3D printing technology to infuse the UTSA-16 metal-forming precursor (Co) into a kaolin-based monomer, followed by internal growth *via* solvothermal synthesis. By systematically varing the cobalt concentration within the kaolin scaffold, they enhanced MOF growth while maintaining the overall mechanical robustness. The resulting composite, containing up to 90 wt% UTSA-16 monomer, exhibited structural and adsorption properties comparable to those of its powdered form, along with enhanced stability. The high adsorption capacity confirmed its strong resemblance to the powdered form, confirming its effectiveness as a gas–solid contactor. Notably, the 3D-printed UTSA-16@10Co-kaolin bulk material exhibited excellent selectively for CO_2 capture over CH_4, N_2, and H_2.

An alternative method involves initially blending an MOF precursor into a slurry to produce a gel suitable for 3D printing. The printed structure is then immersed in a solution containing additional precursors, which react to generate the final MOF. Similar to DIW technology, but distinct from directly incorporating active materials into the ink, the *in situ* growth technique enables nanoscale control over the material's composition, morphology, and structure. Through layer-by-layer or molecular-level growth, it allows for precise tuning of key material characteristics. Building on this concept, Lawson *et al.*[139] successfully fabricated polymer-MOF monoliths by first printing precursor "seeds" and subsequently inducing *in situ* crystal growth. This "print-first, synthesize-after" strategy established an innovative pathway for fabricating polymer-MOF monoliths *via* 3D printing, effectively circumventing the suboptimal rheological properties often associated with MOF-based inks. Further refining this concept, Lawson *et al.*[140] developed a method to form MOF structures by 3D printing gel precursors. In this process, metal ions and organic ligands are mixed with a binder to create a printable gel; while carefully controlled temperature prevents premature metal–ligand coordination. Using this method, they formulated a sol–gel precursors containing ~70 wt% HKUST-1 component. After printing the gel into a 3D structure, the MOF was activated by applying the appropriate reaction temperature, followed by solvent washing to optimize activity. Experimental results show that under optimal conditions, HKUST-1 monoliths produced *via* this Gel Precursor Gel (GPG) method achieve adsorption capacities and adsorbent loadings comparable to DIW-produced counterparts, while demonstrating superior mass transfer kinetics (Fig. 14b).

Although the challenge of poor ink rheology resulting from MOF doping has been partially mitigated, maintaining optimal rheological properties remains a critical hurdle for printing gels intended for *in situ* MOF growth. Liu *et al.*[141] addressed this issue by enhancing the shear-thinning behavior of their hydrogel precursor ink through the incorporation of the nonionic polymer hydroxyethyl cellulose. Their method involved blending precursors for a multifunctional double-network (DN) hydrogel polymer matrix with hydroxyethyl cellulose and MOF ligands to create a printable formulation. The resulting DN hydrogel matrix provides excellent porosity and accessibility, enabling the creation of composites with highly dispersed MOF domains. Characterization of 3D-printed HKUST-1 hydrogel composites, including dye adsorption studies, confirmed the uniform distribution of MOF particles within the DN matrix, leading to high dispersion and enhanced functional performance (Fig. 14c). Similarly demonstrating the advantages of incorporating MOF precursors directly into the ink, Xie *et al.*[142] formulated printable inks by combining gelatin- and GelMA-based hydrogels with transition metal precursors. These inks enabled the direct fabrication of 3D structures *via* 3D printing. To produce 3D-printed single-atom catalysts (SACs), the printed structures were first freeze-dried to remove moisture and then subjected to thermal decomposition. This process anchored metal single atoms onto the carbon derived from the gelatin/gel matrix. The performance of these 3D-printed SACs was evaluated in nitrate reduction reactions, demonstrating their potential utility as efficient electrocatalysts (Fig. 15a).

To promote uniform growth and attain higher MOF loading, the scaffold must provide adequate nucleation sites. Etching the scaffold surface is an effective strategy to increase available nucleation points and expand the internal surface area within the 3D framework. Liu[143] and co-workers employed acetone etching on the surface of a 3D-printed calcium silicate ($CaSiO_3$)/ABS/thermoplastic polyurethane (TPU) alloy scaffold. Following etching, Ca-MOF was directly loaded onto the modified scaffold surface *via in situ* growth. The resulting Ca-MOF/ABS/TPU composite functioned as a promising adsorbent for dye wastewater treatment, exhibiting excellent MB adsorption capacity. Building on this concept of etching-enabled enhancement, Liu[144] *et al.* further employed KOH etching to optimize 3D-printed layered porous structures for maximize active sites exposure. Their approach began with the fabrication of layered porous ceramic scaffolds with tunable porosity using gas-phase silica (SiO_2)-based inks, which exhibited excellent thixotropic and rheological properties for 3D printing. Subsequently, KOH etching was applied to specific SiO_2 nanoparticles within the scaffold, generating additional mesopores. Finally, the iron(III) carboxylate MOF MIL-100(Fe) was deposited onto this functionalized 3D porous structure *via* a modified hydrothermal reaction (Fig. 15b). The resulting 3DP-HPC@MOFs

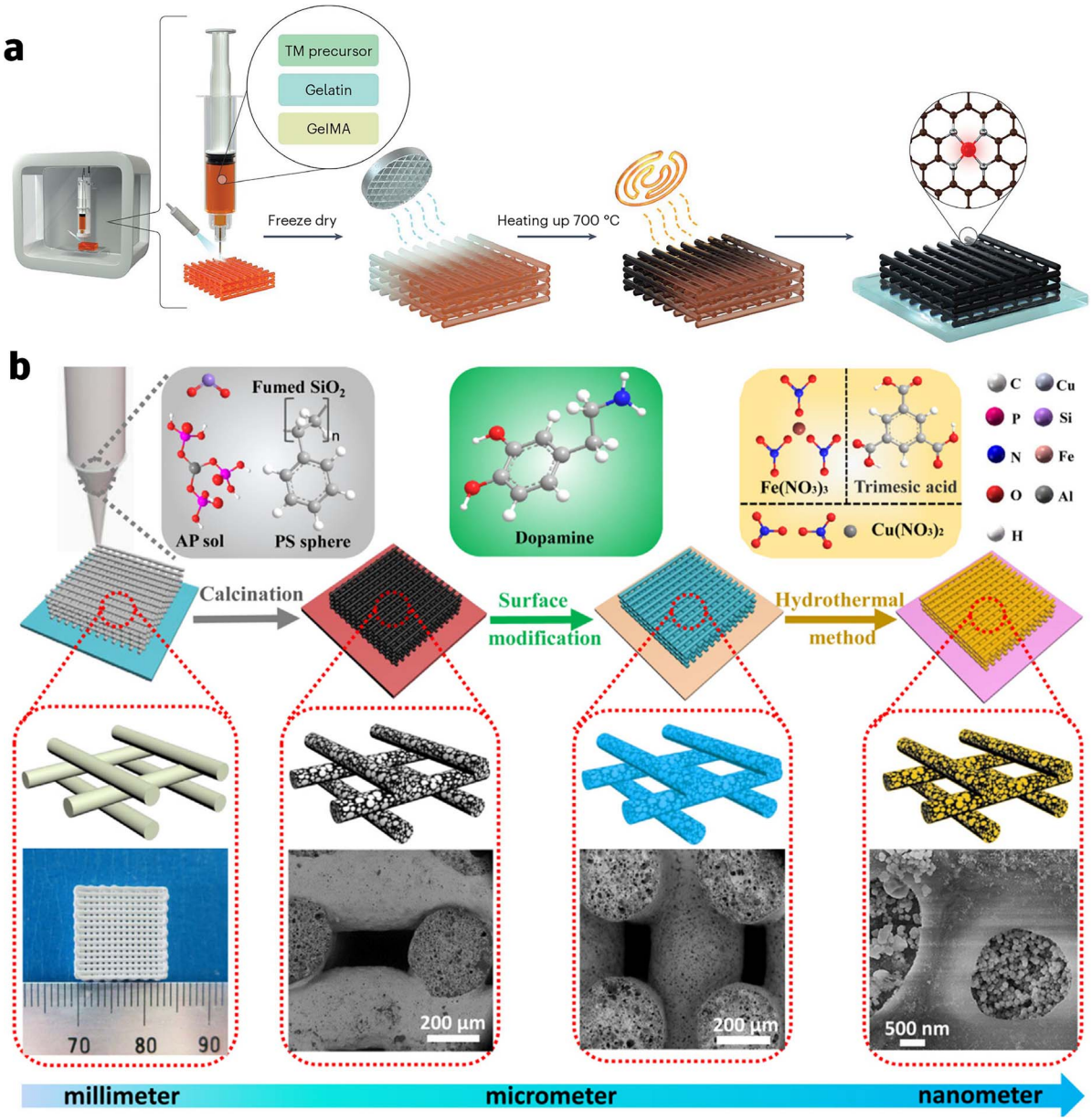

Fig. 15 (a) Layer-by-layer assembly methodology for SAC composites in 3D printing. (b) Multistep architecture design: DIW-processed porous ceramics integrated with spatially ordered metal–organic frameworks.

demonstrated high catalytic activity for sustainable wastewater treatment by effectively degrading multiple organic dyes, including MB, Rh, MG, and CV, without requiring complex separation processes.

A method that relies entirely on the post-processing of 3D-printed structures for the *in situ* growth of MOFs has also been developed for advanced optical sensing platforms. Huang[145] *et al.* developed a dual-component precursor ink comprising organic ligands and common alginates. By leveraging diverse intermolecular and intramolecular hydrogen bonding interactions, this formulation achieved tunable rheological properties and excellent printability. Macroscopic assembly and tunable fluorescence were realized by rapidly immersing the 3D-printed, ligand-containing patterned structures into lanthanide ion solutions, which enabled the swift *in situ* growth of LnMOFs. In a complementary approach demonstrating broader functional versatility, Duan[146] *et al.* employed *in situ* MOF growth on 3D-printed ANF aerogel scaffolds to create high-strength MOF@ANF hybrid aerogel fibers. Within these structures, the MOF crystals exhibited a controlled radial gradient distribution. The deprotonation of the polymeric network increased the local concentration of cobalt ions, thereby promoting MOF crystal growth directly within the ANF strands. The resulting aerogel textiles exhibited exceptional mechanical flexibility, rapid adsorption kinetics, high adsorption capacity, and reliable recyclability, effectively removing diverse pollutants including formaldehyde vapor, heavy metal ions, and organic dyes.

3.2.2 Directly coating. The direct coating method simplifies MOF application onto 3D – printed structures by reducing fabrication time and cost, while accommodating complex geometries. In this approach, MOFs are formulated into low – viscosity inks that enable uniform coverage and effective infiltration into the micropores of the 3D substrate, producing a homogeneous composite. However, insufficient adhesion between the MOFs and 3D-printed structures remains a major technical challenge, often causing coating detachment and compromised performance. Incorporating PVDF into inks has emerged as a primary solution to enhance interfacial bonding. Del Rio[147] *et al.* addressed this issue by suspending dried UiO-66-SO_3H@Ag particles in acetone, blending them with PVDF dissolved in *N*,*N*-dimethylformamide (DMF), and homogenizing the mixture *via* ultrasonication. The ink was then concentrated by acetone evaporation under N_2 flow, 3D-printed onto the substrate, and dried at room-temperature. The resulting device exhibited exceptional reusability (>3 cycles) and effectively treated real water samples, demonstrating high efficiency for radioactive iodine extraction without requiring complex adsorbent recovery procedures. Extending this adhesive approach, Bauzá[148] *et al.* integrated PVDF as a binder into HKUST-1-based inks. The ink was uniformly deposited onto PP substrates to form coatings, which were subsequently hydrophobically functionalized using 1 wt% stearic acid in ethanol. This post-treatment significantly increased water repellency, enabling rapid MB removal (90% within 2 hours) and straightforward regeneration with negligible capacity loss.

To overcome limitations in MOF loading capacity on 3D-printed substrates, an innovative two-step coating strategy has been developed that combines UV-assisted fixation with PVDF-bound secondary layering. Vargas-Muñoz[149] *et al.* established a robust platform by first depositing MIL-100(Fe) onto complex 3D structures, followed by precise UV cross-linking (4-hour curing) to create a covalently anchored base layer. They then enhanced the loading by applying a secondary coating: a PVDF-bound MIL-100(Fe) ink, homogenized *via* solvent processing and uniformly spread over the primed surface. This hierarchical approach proved exceptionally effective for extracting toxic compounds from complex matrices, demonstrating how sequential coating techniques can overcome interfacial limitations. Systematically evaluating such multi-stage strategies, Barzallo[150] *et al.* compared three coating techniques: paste curing, post-treatment, and a combination approach. The paste curing technique involves bringing the 3D-printed device into contact with the MOF, mixing evenly, and then using UV curing to solidify the coating. The post-treatment technique involves dispersing the MOF uniformly in a solvent, then mixing it with a PVDF/DMF solution, and then gently evaporating acetone under a mild nitrogen flow to concentrate the ink. The dispersion is incrementally applied to the pre-cured 3D structure, followed by DMF evaporation to complete the coating process. Tailored for the selective extraction of fluoroquinolones (FQs) in complex wastewater matrices, SEM imaging revealed how different coating approaches influence MOF fixation on the 3D-printed devices. Although the combined technique yielded a slightly enhanced analytical signal for FQs compared to the paste curing method, it required DMF evaporation in an oven, which potentially compromising the device's external structure and leading to uneven MOF distribution. In contrast, the paste curing method is simpler, consumes less carbon material, and minimizes solvent usage, highlighting its practicality for scalable applications.

Beyond interfacial bonding strategies, surface modification of 3D-printed frameworks can significantly enhance MOF adsorption capacity by optimizing deposition efficiency. Fijoł *et al.*[151] demonstrated that acid etching hydrolyzes ester bonds in polymers such as PLA, generating surface hydroxyl and carboxyl groups that elevate hydrophilicity and chemical reactivity, thereby improving MOF anchoring. Concurrently, UV-ozone (O_3) treatment induces photo-oxidation, introducing carbonyl groups that elevate surface charge density and strengthen interactions with cationic species. Both methods fundamentally tailor surface properties to reinforce MOF-scaffold binding while generating hierarchical nano-microscale roughness and porosity. This dual mechanism—combining enhanced chemical reactivity with engineered physical pore structures—provides abundant nucleation sites for MOF capture and retention. Collectively, these modifications boost deposition efficiency and functional performance, extending well beyond what is achievable with interfacial bonding strategies alone.

4 Energy storage application

The rapid advancement of portable electronic devices has intensified the need for efficient small-scale energy storage systems. Extensively employed in areas such as electronics, biotechnology, engineered composites, and energy storage systems, 3D printing is recognized for its reliable manufacturing capability, cost-effectiveness, and design adaptability. This technology has enabled the fabrication of intricate architectures with high structural precision. In particular, 3D printing is an excellent tool for manufacturing EES devices with tailored 3D architectures, as it allows precise control over the electrode thickness, shape and internal porosity. Additionally, 3D printing technology can also introduce porosity into printed objects. Electrodes featuring 3D architectures can greatly improve electrochemical performance, while the selection of optimal active materials and electrolytes can further improve the overall capabilities of energy storage devices.

4.1 Supercapacitor

Supercapacitors offer longer cycle life and greater charge/discharge efficiency compared to conventional batteries. Owing to their compact size, quick response, and excellent durability, micro supercapacitors have become indispensable in portable electronics, sensors, wearable devices, and various other applications that demand rapid charge/discharge cycles and effective energy management. As a result, supercapacitors have emerged as one of the most promising EES devices. The

integration of 3D printed MOF-based electrodes were first applied in lithium-ion supercapacitors. Zhao *et al.*[152] developed a series of graphene-based hybrid composite aerogels by incorporating two-dimensional M-tetrahydroxy-1,4-quinone (M-thq, where M = Cu, Cu/Co, or Cu/Ni) into CNTs@rGO aerogel electrodes. These porous aerogels, featuring a periodic microlattice constructed from multi-dimensional components, maintain excellent structural stability even under moderate deformation. The inherent porosity of these 3D printed microlattice electrodes significantly enhances electron and ion transfer pathways. In particular, the Cu/Co-THQ@CNTs@rGO aerogel cathode combined with the C_{60}@VNNWs@rGO aerogel anode achieves a maximum gravimetric capacitance of 178.68 F g−1 and a remarkable gravimetric energy density of 396.89 Wh kg−1, alongside excellent cycling stability (Fig. 16a). Catarineu *et al.*[153] also applied 3D printing to fabricate microporous cathode materials for zinc-ion hybrid capacitors using the zinc imidazolate framework (ZIF-8). When assembled with a zinc foil anode, the resulting zinc-ion hybrid capacitor exhibits outstanding electrochemical performance, achieving a record areal capacitance of 16.9 F cm−2 and an impressive areal energy density of 7.23 mWh cm−2 (Fig. 16b). The introduction of pyridinic nitrogen *via* the imidazole linker enhances both ion affinity and electrical conductivity. Moreover, the hierarchical porosity of the 3D-printed structure, combined with the microporosity and high surface area preserved from ZIF-8 during pyrolysis, creates optimal pathways for efficient ion transport and insertion. During pyrolysis, the 3D-printed ZIF-8 lattice transforms into a conductive, graphite-like network while maintaining its advantageous structural features. Additionally, the strategy of *in situ* growth on 3D-printed surfaces followed by carbonization has also been proven effective for fabricating high-performance supercapacitor electrodes. Chuang *et al.*[154] grew Ce-MOF on the surface of 3D-printed CNC hydrogel enriched with terminal hydroxyl groups, followed by carbonization treatment. Owing to the pseudocapacitive nature of CeO_2, the resulting Ce-MOF-derived nanocomposite electrodes, composed of CeO_2 and carbon, exhibit excellent electrochemical properties. At a charge–discharge current density of 0.5 mA cm−2, the areal capacitance reaches 43 mF cm−2, primarily attributed to the pseudocapacitance of the MOF-derived CeO_2.

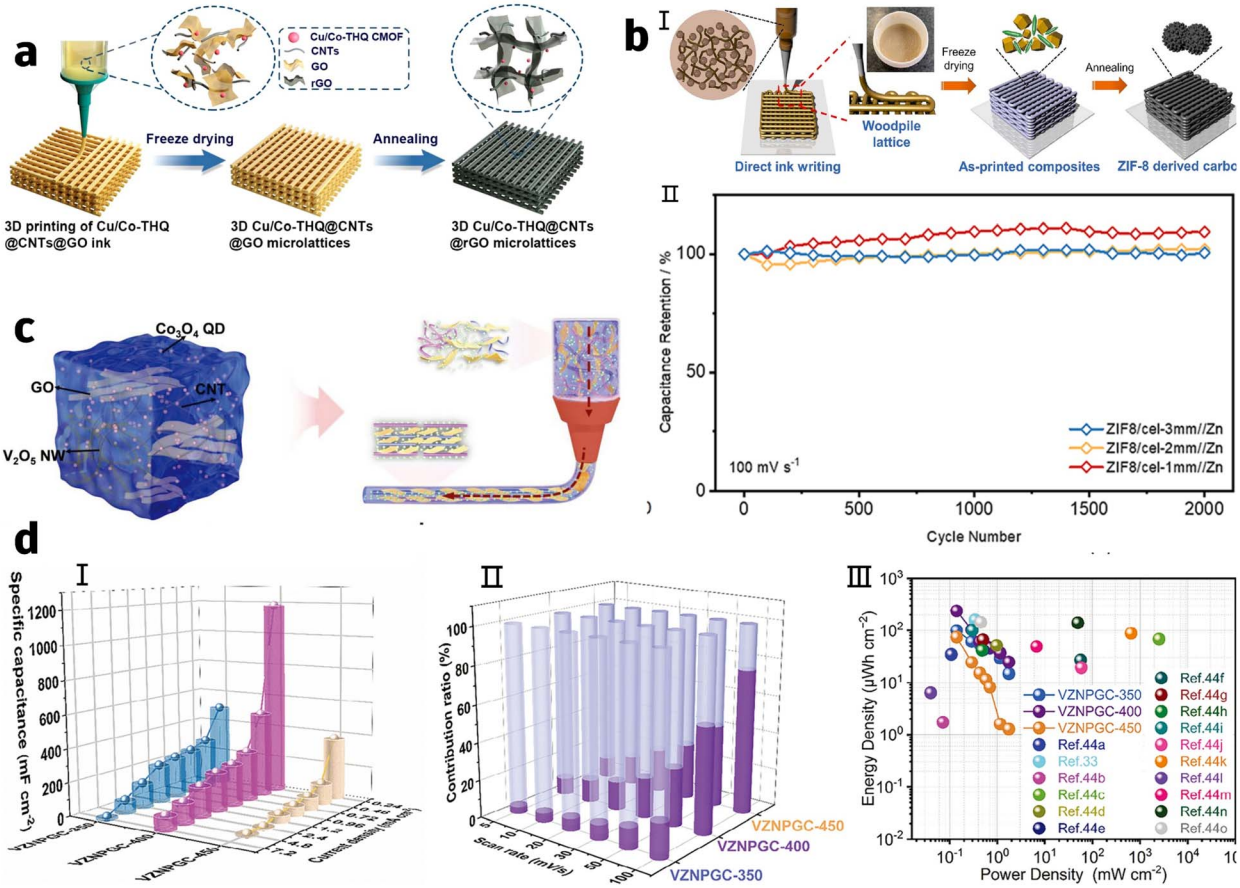

Fig. 16 (a) The structural illustration depicts both the fabricated microlattice architecture and the flow behavior characteristics of Cu/Co-THQ@CNTs@GO composite ink slurries. (b) (I) Additive manufacturing methodology for ZIF-8-based functional inks. (II) Comparative cycling durability evaluation of cellulose-ZIF-8//Zn electrochemical architectures (1–3 mm thickness variations) under 100 mV s−1 scan rate conditions. (c) Process schematic illustrating the additive manufacturing methodology for 3D-printable VCGQD hydrogel-based electrode architectures. (d) Electrochemical performance: the three-electrodes: (I) Comparison of specific capacitance. (II) The capacitive contribution of VZNPGC//MXene MSCs. (III) Ragone plot.

Researchers further improved the electrochemical performance of 3D-printed supercapacitors by modifying the printed materials. The work by Zhou *et al.*[155] demonstrates that incorporating V_2O_5 nanowires (NWs) with liquid crystal properties enables the formation of a controllable layered structure. The incorporation of 0D Co_3O_4 quantum dots with pseudocapacitive characteristics into the interconnected porous framework further amplifies the synergistic effect between the two components (Fig. 16c). This design not only improves the electrode's electrochemical performance but also boosts the material's stability and operability. At a current density of 0.24 mA cm−2, the resulting electrode achieves an areal capacitance of 306.13 mF cm−2 and delivers an energy density is 34.44 μWh cm−2 at a power density of 0.108 mW cm−2. In a relatetd study, Zhou *et al.*[74] demonstrated that the introduction of Ni ions has a effectively facilitates the phosphorization process, helping to preserve the original structural of the nano-MOF composite. Furthermore, theoretical calculations further revealed that metal phosphides exhibit excellent electrical conductivity, while the formation of phosphorus-containing phases can effectively enhance the conductivity of the composite. By integrating stable hollow nano-MOF architectures with suitable metal ions, the electrochemical performance of 3D-printed MSCs can be substantially improved. MSC employing hollow nano NiCo bimetallic phosphide composites as the cathode active material achieved an areal capacitance of 1184 mF cm−2 at a current density of 0.24 mA cm−2, along with an energy density of 236.75 μWh cm−2 at a power density of 0.14 mW cm−2 (Fig. 16b).

In conclusion, the integration of 3D printing into the fabrication of micro-supercapacitors has reached a highly advanced level (Table 1). The printed lattice structures notably reduce ion diffusion resistance and shorten the diffusion distance, which in turn leads to a marked improvement in electrochemical performance. 3D printing technology can further refine the electrode structure of supercapacitors. In addition, printable materials that enhance energy density and power density have been investigated. Overall, the combination of 3D printing and the development of new materials is driving the advancement of supercapacitor technology towards higher energy density, higher power density, and more complex structures, while simultaneously reducing manufacturing costs. This facilitates its widespread application in fields such as energy storage and smart devices.

4.2 Batteries

Leveraging the versatility of 3D printing, electrode designs can be precisely tailored to meet the requirements of specific electrochemical systems, rendering them well-suited for a wide range of energy storage devices (Table 2). Lyu *et al.*[156] utilized extrusion-based 3D printing to fabricate cobalt-based Co-MOF, which were subsequently annealed to yield hierarchically porous carbon frameworks embedded with Co nanoparticles. When applied in lithium-oxygen batteries, the porous architecture significantly facilitated the deposition and decomposition of Li_2O_2 particles, significantly enhancing practical specific energy reaching up to 798 Wh kg−1 cell. In a follow-up study, Lyu *et al.*[157] employed 3D printing to construct Zn-MOFs, which were carbonized to form N-doped carbon framework for lithium-ion batteries. The 3D-printed electrode exhibited an ultra-high areal capacity of 30 mA h cm−2 at a high current density of 10 mA cm−2, an impressive cycle life of ∼2000 hours and a stable average coulombic efficiency (CE) of 97.9% at 1 mA cm−2. Beyond electrodes, 3D printing has also been harnessed to fabricate MOF-based hybrid solid-state electrolyte, further enhance the electrochemical performance of the battery (Fig. 17a). Li *et al.*[158] used 3D printing technology to fabricate

Table 1 Application of 3D printing materials in supercapacitors[a]

Sample	Electrolyte	CD/SS	SC	ED	PD	Ref.
VCGQD-2//MXene	PVA-KOH gel	0.48 mA cm−2	0.30613 F cm−2	34.44 μWh cm−2	0.108 mW cm−2	149
VZNPGC//MXene	PVA-KOH gel	0.24 mA cm−2	1.184 F cm−2	236.75 μWh cm−2	0.14 mW cm−2	108
LIHC	LiPF6/EC/DMC	0.05 A g−1	2.99 F cm−2	396.89 Wh kg−1	1999.90 W kg−1	146
ZIF8/cel-3 mm//Zn	2 M zinc sulfate	5 mA cm−2	16.9 F cm−2	7230 μWh cm−2	34.67 mW cm−2	147
CeOx/CM-900	0.5 M Na_2SO_4	0.5 mA cm−2	0.043 F cm−2	—	—	148

[a] CD: current density; ED: energy density; PD: power density; SC: specific capacitance; SS: scan speed.

Table 2 Application of 3D printing materials in batteries[a]

Types	Material	CD/SS	Capability	SL	Ref.
Li–O2	Li/3DP-LiFePO4	10 mA cm−2	30 mA h cm−2	—	151
	Co-mof	0.8 mA cm−2	525 mA h g−1	—	150
Na–S	Y SAs/NC	0.1 A g−1	822 mA h g−1	6.5 mg cm−2	153
Li–S	Al-MOF-160/S	0.1 C	966 mA h g−1	2.73 mg cm−2	154
ZIBs	UiON-PHC	0.1 A g−1	128 mA h g−1	—	156
ZIBs	3DP-VO@Ti	0.1 A g−1	7.28 mA h cm−2	—	155
ZIBs	MXene/Cu-THBQ	0.2 A g−1	235.4 mA h g−1	—	157

[a] Units that cannot be converted are presented as they are in the original data.

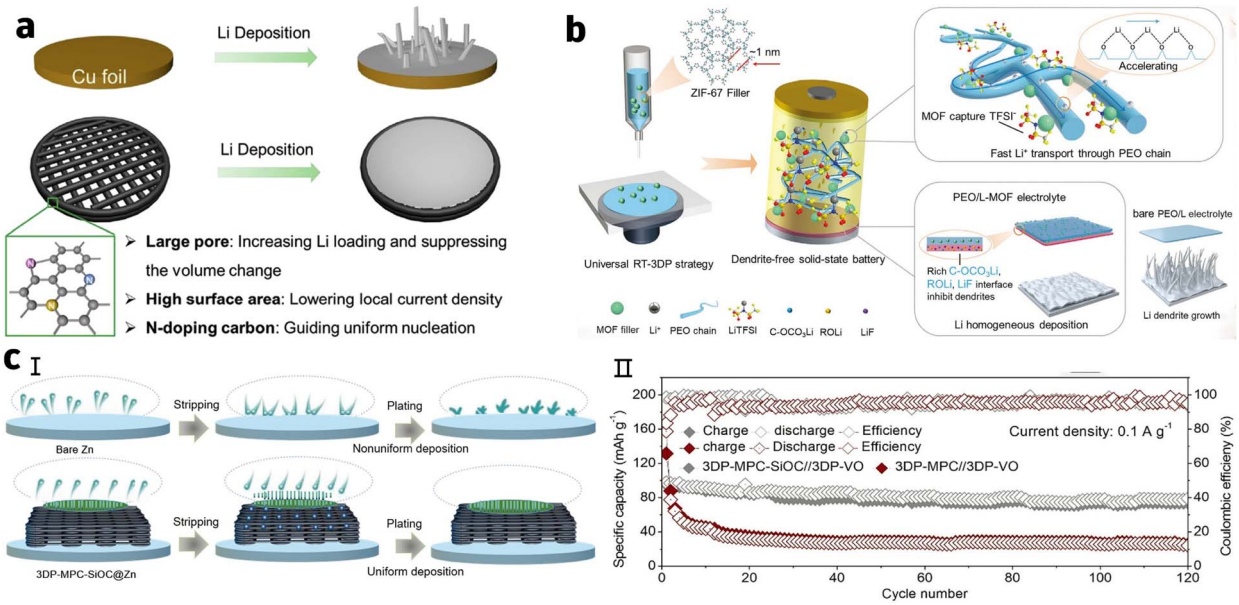

Fig. 17 (a) The 3D carbon host anode enables dendrite-free lithium deposition, high rate capability, and high areal capacity, outperforming traditional copper foil-based anodes. (b) Universal RT-3DP strategy employs HSSE ink (PEO/MOF/LiTFSI) to fabricate dendrite-free solid-state lithium batteries, enabling enhanced ionic conductivity and long-term cyclability, surpassing conventional pure PEO-based systems. (c) (I) Schematic illustration of dendritic growth mechanisms on bare Zn *versus* 3D-printed MPC-SiOC anodes. (II) Comparative long-cycling performance of 3DP-MPC-SiOC@Zn//3DP-VO@Ti *vs.* conventional 3DP-MPC@Zn//3DP-VO@Ti batteries, demonstrating enhanced stability *via* optimized electrode design.

a 3D-printed hybrid electrolyte with dendrite suppression properties. After 70 charge–discharge cycles, the fabricated battery maintained a discharge capacity of 134 mA h g−1 (Fig. 17b).

The "polysulfide shuttle effect" in sulfur-based batteries is a key issue that affects battery performance, particularly energy efficiency and cycling stability. Designing 3D-printed electrode structure can effectively reduce the polysulfide shuttle effect. Zhang *et al.*[159] synthesized Y single-atom doped N-doped carbon polyhedra (Y SAs/NC) and constructed a full battery. This fully charged Na–S battery delivered a high capacity of 822 mA h g−1 and demonstrated exceptional durability, retaining 97.5%of its capacity after more than 1000 cycles at a high current density of 5 A g−1. The introduction of atomic Y sites, combined with a 3D electrode architecture, synergistically accelerate reaction kinetics and effectively alleviate the "shuttle effect". Containing polysulfide migration phenomena represents a critical frontier for advancing lithium-sulfur battery technology, as strategic inhibition of active material crossover directly correlates with enhanced specific energy retention and extended electrochemical cyclability. Xi *et al.*[160] engineered a hierarchically porous Al-MOF/S composite cathode through DLP-based 3D printing, creating coordinated macro-mesoscale pore networks that synergistically address multiple performance limitations in lithium-sulfur systems. The triply periodic minimal surface architecture optimizes interfacial dynamics by simultaneously enabling efficient electrolyte permeation, establishing low-tortuosity charge transfer pathways, confining polysulfide species *via* molecular-scale sieving, and accommodating volumetric strain during cycling. This architectured cathode achieved an areal sulfur loading of 2.73 mg cm−2 and demonstrated outstanding electrochemical persistence, maintaining a specific capacity of 504 mA h g−1 with 98.2% CE over 300 cycles at a rate of 0.5 C.

A major challenge in zinc-ion batteries is the formation of zinc dendrites, which arises from uneven zinc deposition on the electrode surface and leads to the growth of needle-like or tree-like zinc metal structures. To tackle this issue, Idrees[161] and collaborators engineered a 3D printed lattice framework for anode optimization. This engineered structure promotes homogeneous charge distribution across the electrode surface, effectively mitigating polarization effects and enhancing operational durability. The modified zinc-based cells maintained a specific capacity of 78.8 mA h g−1 with a charge efficiency 94.04% at a current density under 0.1 A g−1. Furthermore, the system demonstrated robust energy storage performance, maintaining stable operation over 120 charge–discharge cycles and achieving specific mass-specific energy and power metrics of 41 Wh kg−1 and 1.2 W kg−1, respectively, when calculated against full electrode mass (Fig. 17c). Batool *et al.*[162] employed 3D printing to develop a compositionally graded anode architecture that facilitated homogeneous Zn2+ ion flux *via* depth-varying porosity. This design improved electrochemical reversibility during metal deposition/dissolution cycles and mechanically stabilized interfacial dynamics, effectively suppressing dendritic propagation. The optimized cell configuration maintains 122 mA h g−1 (88.6% capacity preservation) across extended cycling while delivering gravimetric energy metrics of 34.6 Wh kg−1 and specific power output of 69.1 W kg−1 under operational loads. Notably, this system also

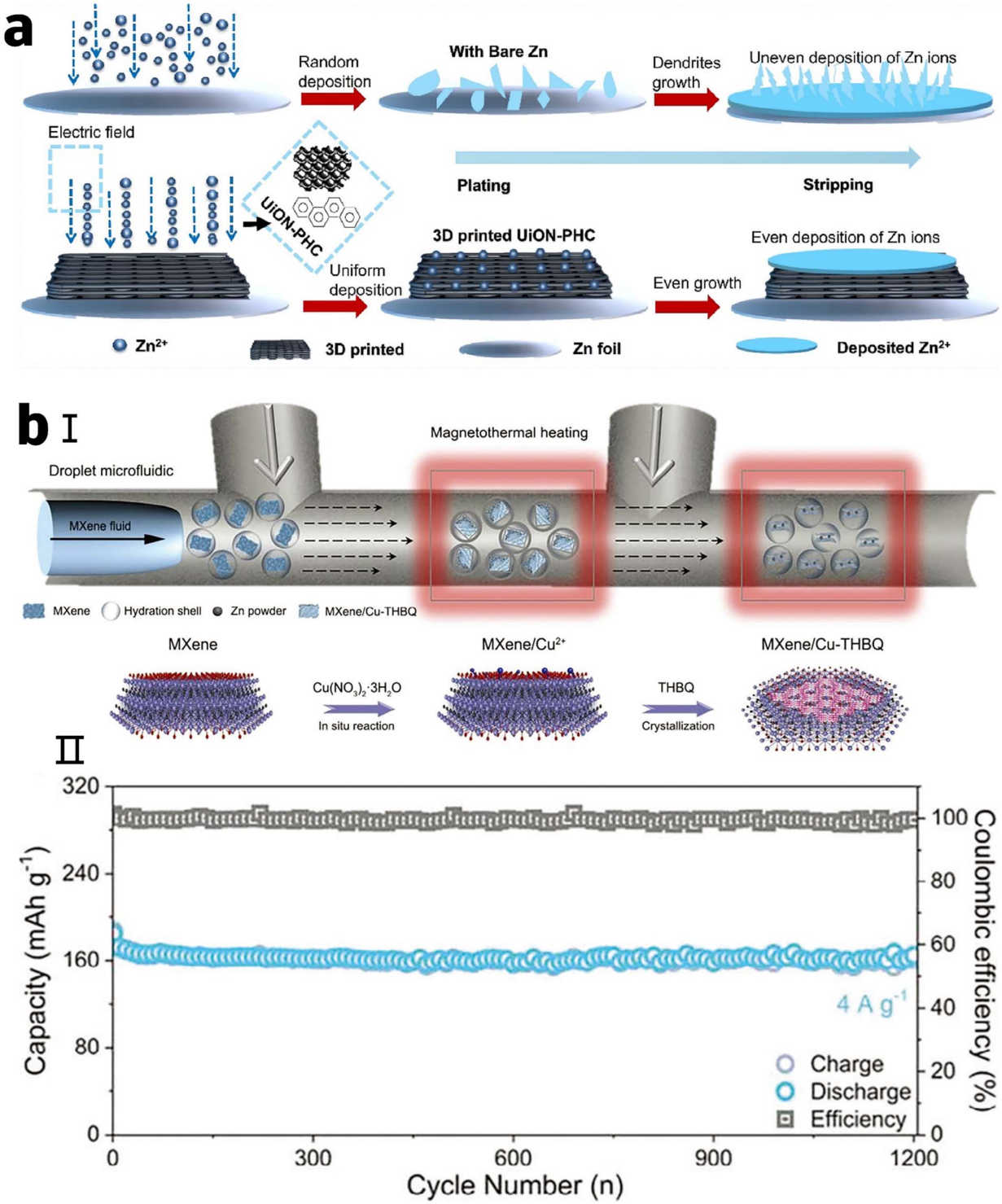

Fig. 18 (a) Schematic illustration of Zn2+ deposition mechanisms on bare Zn *versus* 3D-printed UiON-PHC composite anodes. (b) (I) Microfluidic synthesis of MXene/Cu-THBQ/Zn-P printable hybrid ink and heterostructured composite formation mechanism. (II) Long-term cycling performance (4 A g−1) of M3DP-MXene/Cu-THBQ/Zn-P//G-TEMPO full battery, demonstrating high-rate stability and extended lifespan.

achieved a surface-normalized capacity of 85.1 mA h cm−2 with a charge transfer efficiency of 94.8%, demonstrating simultaneous improvements in both planar and volumetric electrochemical performance parameters (Fig. 18a). Beyond dendrite suppression, hydrogen evolution is another persistent side reaction in zinc-ion batteries, especially at high voltages. By precisely designing the porous structure of the electrode *via* 3D printing, this unwanted hydrogen evolution can be effectively mitigated. Lu *et al.*[163] used microfluidic-assisted 3D printing to fabricate a corrosion-resistant Zn-Power-based anode featuring

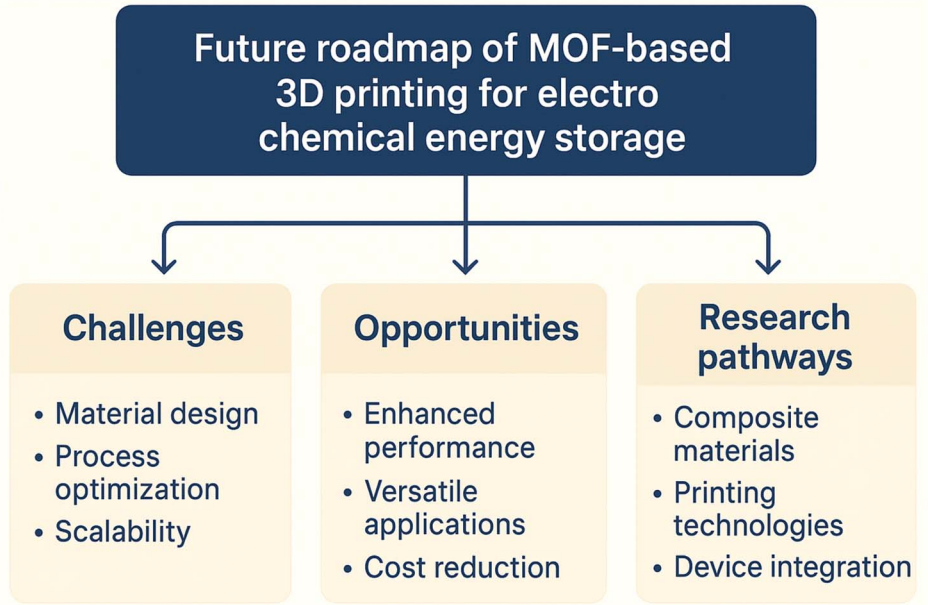

Fig. 19 Future roadmap of MOF-based 3D printing for electrochemical energy storage.

heterogeneous structure forming functional layers. This architecture effectively suppressed the hydrogen evolution reaction during the repeated zinc plating/stripping cycles, ensuring stable Zn cycling. Their M3DP-MXene/Cu-THBQ/Zn-P anode operated reliably in a symmetric cell at a current density of 2 mA cm−2 for 1800 hours, with a lifespan nearly 11 times longer than that of a bare Zn–P symmetric cell and an average CE of 99.5% at 5 mA cm−2. When assembled with a 3D-printed G-TEMPO cathode aerogel, the zinc-organic full battery delivered excellent cycling stability, retaining approximately 96.8% of its capacity after 1200 cycles at 4 A g−1 (Fig. 18b).

In summary, 3D printing has found extensive application across various battery research fields, including lithium-ion, sulfur-based, zinc-ion, and other emerging battery technologies. By adjusting the printing parameters, the microscopic structure of the electrode can be tailored to enhance conductivity, increase specific surface area, and optimize ion transport rate. This approach effectively inhibits the polysulfide shuttle phenomenon in sulfur-based batteries and suppresses zinc dendrites formation in zinc-ion batteries. The technologies significantly improve cycling stability, safety, energy density, and overall efficiency, thereby extending battery lifespan and minimizing performance degradation over repeated charge–discharge cycles. Additionally, they can help reduce safety risks and enhance the operational reliability of the batteries in various applications.

5 Conclusions and outlook

Flexible and conductive MOF materials have been developed by incorporating flexible ligands (*e.g.*, N-donor ligands, quinone-based ligands) and composite conductive materials (*e.g.*, polyaniline, carbon nanotubes), substantially improving their mechanical flexibility and electrochemical performance while achieving high cycling stability and capacity in lithium-ion batteries and supercapacitors. Thermally stable and conductive MOFs have been engineered through multi-dimensional structural design (*e.g.*, 2D layered frameworks, 3D helical networks) and ligand functionalization (*e.g.*, amino modification), enhancing thermal stability and enabling applications in high-temperature catalysis and gas adsorption. High-strength MOF materials have been realized through interface reinforcement (*e.g.*, MOF-polymer composites) and topological structural engineering (*e.g.*, 3D cross-linked networks), which boost mechanical robustness and ion transport efficiency, making them promising candidates for solid-state electrolytes and advanced electrode materials.

In terms of 3D printing strategies for MOFs: DIW enables precise patterning of complex electrode structures and significantly enhances the energy and power densities of energy storage devices by tailoring the rheological properties (*e.g.*, shear-thinning behavior) of MOF inks and employing high solid loading designs. FDM fabricates conductive composite filaments by combining MOFs with thermoplastic polymers (*e.g.*, PLA, ABS), but its performance is often constrained by the inherent low conductivity of the polymer matrix and the thermal instability of MOFs. DLP/SLA printing harnesses the synergistic effects between photocurable resins and MOFs to fabricate high-resolution porous structures suitable for micro-supercapacitors and catalytic supports. SLS develops multi-layer architectures with open porosities by integrating MOF-polymer composite powders with laser sintering technology, though its scalable application still requires further breakthroughs. Overall, 3D printing technologies have opened up new possibilities for the designing and deploying functional MOF materials.

In addition to the 3D printing techniques themselves, post-processing approaches are equally crucial for realizing high-

performance MOF materials. Among them, the *in situ* growth approach enable direct synthesis of MOFs on 3D printed templates, addressing challenges such as poor ink rheology while increasing MOF loading and achieving uniform distribution. Alternatively, direct coating involves depositing MOF dispersions onto the surface of 3D printed substrates, which simplifies fabrication but requires careful interfacial engineering to prevent delamination and maintain coating integrity. Together, these post-processing strategies provide effective solutions for 3D printed MOFs, further expanding their application prospects in batteries and supercapacitors.

3D printed MOF materials have shown great application prospects in batteries and supercapacitors. In supercapacitors, MOF-derived porous carbon electrodes exhibit high specific capacitance (178.68 F g−1) and energy density (396.89 Wh kg−1), with their hierarchical porous structure facilitating rapid ion transport. For batteries, 3D printed electrodes in lithium-sulfur batteries suppress the polysulfide shuttle effect, achieving high sulfur loading (2.73 mg cm−2) and extended cycling lifespan (504 mA h g−1 over 300 cycles). In zinc-ion batteries, the gradient porous structure mitigate dendrite formation, enhancing the cycling stability to over 1800 hours. Collectively, these results highlight the potential of 3D-printed MOFs as next-generation materials for high-energy-density and long-cycle-life green energy storage.

As a forward-looking perspective, this section highlights the future directions and intelligent evolution of 3D-printed MOF technologies for electrochemical energy storage. Despite their significant potential, the direct 3D printing of MOFs still faces inherent challenges, including unsuitable rheological properties that hinder smooth extrusion and cause nozzle clogging, improper curing, and cracked electrodes. Further obstacles involve ensuring long-term cycling stability, achieving scalable ink production, and managing the cost of functional ligands. To overcome these limitations and drive future advancements, research is expected to increasingly leverage machine learning for optimizing ink design, developing multi-material printing for complex device architectures, and promoting system-level integration of MOF-based electrodes. Machine learning can predict optimal MOF compositions and reaction conditions, enabling rapid screening of high-performance materials, while data-driven modeling can guide the design of inks with tailored rheology and conductivity. Moreover, deep learning models will correlate process parameters (*e.g.*, ink rheology, curing conditions) with device performance (*e.g.*, porosity, ion transport efficiency), enabling autonomous optimization for batteries and supercapacitors. Generative adversarial networks (GANs) will empower inverse design of hierarchical porous structures customized for specific energy demands, and the integration of digital twins with closed-loop experimental systems will bridge multi-scale modeling gaps. Ultimately, adopting a property-oriented design framework—strategically aligning MOF properties such as mechanical flexibility, electrical conductivity, and thermal stability with 3D printing techniques will accelerate the transition from experience-driven to data-driven innovation, paving the way for next-generation, high-performance MOF-based energy devices (Fig. 19).

Abbreviations

MOFs	metal–organic frameworks
DIW	direct ink writing
FDM	fused deposition modeling
DLP	digital light processing
SLS	selective laser sintering
EES	electrochemical energy storage
SLA	stereolithography apparatus
LIBs	lithium-ion batteries
AMOF	amorphous MOF
LMCT	ligand-to-metal charge transfer
AP	ammonium perchlorate
MPCA	carbon nanotube aerogel
NIPS	non-solvent-induced phase separation
2-HEA	2-hydroxyethyl acrylate
TEGDA	tetraethylene glycol diacrylate
GPG	gel precursor gel
SACs	single-atom catalysts
DMF	*N*,*N*-dimethylformamide
NWs	nanowires
PP	polypropylene
SiC	silicon carbide
Fe-MOF	iron MOF
NMP	*N*-methyl-2-pyrrolidone
MSC	micro-supercapacitor
GO	graphene oxide
CNTs	carbon nanotubes
PLA	polylactic acid
PCL	polycaprolactone
ABS	acrylonitrile butadiene styrene
CF	carbon fibers
RT-OP	room-temperature phosphorescence
TPP	two-photon polymerization
GelMA	methacrylated gelatin
MB	methylene blue
DN	double-network
TPU	thermoplastic polyurethane
FQs	fluoroquinolones
CE	coulombic efficiency

Author contributions

Chenfei Zhou: conceptualization, writing – original draft. Huijie Zhou: conceptualization, writing – review & editing. Xinyu Qin: resources, writing – review & editing. Shunyu Gu: data curation, formal analysis, writing – review & editing. Mengyao Zhang: data curation, formal analysis, writing – review & editing. Jifan Chen: writing – review & editing. Lingfeng Zhai: writing – review & editing. Huan Pang: supervision, writing – review & editing.

Conflicts of interest

The authors declare that they have no known competing financial interests or personal relationships that could have appeared to influence the work reported in this paper.

Data availability

No primary research results, software or code have been included and no new data were generated or analysed as part of this review.

Acknowledgements

This study was supported by the National Natural Science Foundation of China (NSFC-22509178, 52371240) and the China Postdoctoral Science Foundation (2025M770225), Yangzhou Innovation Capability Enhancement Program (YZ2022170).

References

1 A. K. Sampene, C. Li and T. K. Nsiah, *Energy Strategy Rev.*, 2024, **53**, 101388.
2 S. Ergun, A. Dik, R. Boukhanouf and S. Omer, *Sustainability*, 2025, **17**, 1311.
3 R. Tao, Y. Gu, Z. Du, X. Lyu and J. Li, *Nat. Rev. Clean Technol.*, 2025, **1**, 116–131.
4 O. M. Yaghi and H. Li, *J. Am. Chem. Soc.*, 1995, **117**, 10401–10402.
5 X. Zhang, M. Yan, P. Chen, J. Li, Y. Li, H. Li, X. Liu, Z. Chen, H. Yang, S. Wang, J. Wang, Z. Tang, Q. Huang, J. Lei, T. Hayat, Z. Liu, L. Mao, T. Duan and X. Wang, *The Innovation*, 2025, **6**, 100778.
6 T. Shaikh, S. Pise, R. Bhosale, M. Vadiyar, K.-W. Nam and S. Kolekar, *Energy Fuels*, 2025, **39**, 2396–2421.
7 P. D. Patil, N. Gargate, M. S. Tiwari and S. S. Nadar, *Int. J. Biol. Macromol.*, 2025, **291**, 138984.
8 Q. Li, G. Yuan, T. Pan, Y. Wang, Y. Xu and H. Pang, *Int. J. Hydrogen Energy*, 2024, **93**, 338–345.
9 S. Wang, Y. Su, Z. Jiang, Z. Meng, T. Wang, M. Yang, W. Zhao, H. Chen, M. Shakouri and H. Pang, *Nano Lett.*, 2024, **24**, 15101–15109.
10 Y. Shi, G. Song, B. Yang, Y. Tang, Z. Liu, Z. Zhang, M. Shakouri, J. Cheng and H. Pang, *Adv. Mater.*, 2025, 2416665.
11 Y. Su, J. Hu, G. Yuan, G. Zhang, W. Wei, Y. Sun, X. Zhang, Z. Liu, N. Suen, H. Chen and H. Pang, *Adv. Mater.*, 2023, **35**, 2307003.
12 Y. Tang, Y. Shi, Y. Su, S. Cao, J. Hu, H. Zhou, Y. Sun, Z. Liu, S. Zhang, H. Xue and H. Pang, *Adv. Sci.*, 2024, **11**, 2403802.
13 Y. Pi, H. Lin, Z. Meng, Z. Qiu, Y. Su, X. Hang and H. Pang, *Chem. Eng. J.*, 2024, **499**, 155618.
14 G. Yuan, Y. Su, X. Zhang, B. Gao, J. Hu, Y. Sun, W. Li, Z. Zhang, M. Shakouri and H. Pang, *Natl. Sci. Rev.*, 2024, **11**, nwae336.
15 Y. Su, Y. Zhang, G. Yuan, Y. Tang, G. Zhang, M. Shakouri, H.-C. Chen, H. Zhou, Z. Liu and H. Pang, *Sci. China Chem.*, 2025, **68**, 2958–2966.
16 S. He, B. Hollenbeck, G. Overgoor, D. Proserpio and A. Tosyali, *Proc. Natl. Acad. Sci. U. S. A*, 2022, **119**, e2211932119.
17 A. Felix Sahayaraj, H. Joy Prabu, J. Maniraj, M. Kannan, M. Bharathi, P. Diwahar and J. Salamon, *J. Inorg. Organomet. Polym.*, 2023, **33**, 1757–1781.
18 X. Li, K. Chen, R. Guo and Z. Wei, *Chem. Rev.*, 2023, **123**, 10432–10467.
19 B. Zhu, S. He, Y. Yang, S. Li, C. H. Lau, S. Liu and L. Shao, *Nat. Commun.*, 2023, **14**, 1697.
20 S. Zhou, O. Shekhah, A. Ramírez, P. Lyu, E. Abou-Hamad, J. Jia, J. Li, P. M. Bhatt, Z. Huang, H. Jiang, T. Jin, G. Maurin, J. Gascon and M. Eddaoudi, *Nature*, 2022, **606**, 706–712.
21 Z. Zhang, Y. Liu, R. Zhu and H. Pang, *Inorg. Chem. Commun.*, 2024, **168**, 112784.
22 Y. Sun, T. Huang, W. Feng, G. Zhang, H. Ji, Y. Zhu, H. Zhou, F. Dou, Y. Su, Z. Liu, M. Yang and H. Pang, *Inorg. Chem.*, 2024, **63**, 24876–24884.
23 H. Yao, F. Wang, H. Chong, J. Wang, Y. Bai, M. Du, X. Yuan, X. Yang, M. Wu, Y. Li and H. Pang, *Adv. Sci.*, 2023, **10**, 2300601.
24 H. Wang, X. Cui, Z. Gao, H. Shi and F. Liu, *J. Phys. Chem. Solids*, 2024, **187**, 111876.
25 L. Zhou, W. Ning, C. Wu, D. Zhang, W. Wei, J. Ma, C. Li and L. Chen, *Adv. Mater. Technol.*, 2019, **4**, 1800402.
26 Y. Wang, T. Pan, G. Yuan, Q. Li and H. Pang, *Compos. Commun.*, 2024, **52**, 102144.
27 W. Wang, D. Chen, F. Li, X. Xiao and Q. Xu, *Chem*, 2024, **10**, 86–133.
28 C. Yan, J. Wei, J. Guan, Z. Shao and S. Lv, *Carbon*, 2023, **213**, 118187.
29 Z. Li, X. Yang, C. Ju, T. Tian, J. Hou, Z. Hu and J. Zou, *Mater. Sci. Eng. R Rep.*, 2026, **167**, 101123.
30 S. Liang, G. Wang, L. Dong, X. Yang, B. Zhou, Z. Duan, Z. Xie and Y. Hu, *Appl. Surf. Sci.*, 2025, **681**, 161602.
31 S. Mahmud, M. Rahman, M. Kamruzzaman, M. O. Ali, M. S. A. Emon, H. Khatun and M. R. Ali, *Results Eng.*, 2022, **15**, 100472.
32 Q. Chai, Z. Liu, Z. Deng, Z. Peng, X. Chao, J. Lu, H. Huang, S. Zhang and Z. Yang, *Nat. Commun.*, 2025, **16**, 1633.
33 Z. Wei, Y. Shi, P. Li, M. Gao, X. Zhang, H. Pan and C. Liang, *J. Colloid Interface Sci.*, 2025, S0021979725004515.
34 R. Naik, H. P. Nagaswarupa, H. C. Ananda Murthy and M. E. T. Sillanpää, *Advanced Nanomaterials for Energy Storage Devices*, Springer Nature Switzerland, Cham, 2024.
35 S. J. An, Y. Zhu, S. H. Lee, M. D. Stoller, T. Emilsson, S. Park, A. Velamakanni, J. An and R. S. Ruoff, *J. Phys. Chem. Lett.*, 2010, **1**, 1259–1263.
36 M. Imran, T. Hussain, U. Shuaib, F. E. Mubarik, M. Tahir, M. A. Toheed, A. Hussnain and I. Shakir, *Ionics*, 2025, **31**, 3631–3641.
37 Z. Chen, Y. Yang, S. Xie, Y. Liu, P. Liang, X. Hu and Z. Wen, *J. Energy Chem.*, 2025, **103**, 237–263.
38 C. Zhu, T. Liu, F. Qian, W. Chen, S. Chandrasekaran, B. Yao, Y. Song, E. B. Duoss, J. D. Kuntz, C. M. Spadaccini, M. A. Worsley and Y. Li, *Nano Today*, 2017, **15**, 107–120.
39 L. Li, J. Meng, X. Bao, Y. Huang, X. Yan, H. Qian, C. Zhang and T. Liu, *Adv. Energy Mater.*, 2023, **13**, 2203683.

40 V. Dananjaya, S. Marimuthu, R. (Chunhui) Yang, A. N. Grace and C. Abeykoon, *Prog. Mater. Sci.*, 2024, **144**, 101282.
41 Y. Ren, F. Meng, S. Zhang, B. Ping, H. Li, B. Yin and T. Ma, *Carbon Energy*, 2022, **4**, 446–457.
42 L. Zeng, H. He, H. Chen, D. Luo, J. He and C. Zhang, *Adv. Energy Mater.*, 2022, **12**, 2103708.
43 T. Bashir, S. Zhou, S. Yang, S. A. Ismail, T. Ali, H. Wang, J. Zhao and L. Gao, *Electrochem. Energy Rev.*, 2023, **6**, 5.
44 T. Meng, D. He, Z. Han, R. Shi, Y. Wang, B. Ren, C. Zhang, Z. Mao, G. Luo and J. Deng, *Nano-Micro Lett.*, 2024, **16**, 246.
45 M. Nehra, N. Dilbaghi, G. Marrazza, A. Kaushik, R. Abolhassani, Y. K. Mishra, K. H. Kim and S. Kumar, *Nano Energy*, 2020, **76**, 104991.
46 J. P. Mensing, T. Lomas and A. Tuantranont, *Sustain. Mater. Technol.*, 2020, **25**, e00190.
47 Y. Wang, J. Liu, X. Ma and X.-J. Liang, *Nano Res.*, 2018, **11**, 2932–2950.
48 D. Kim, Q. T. T. Nguyen, S. Lee, K.-M. Choi, E.-J. Lee and J. Y. Park, *npj Microgravity*, 2023, **9**, 63.
49 C. Sun, J. Zhong, Z. Gan, L. Chen, C. Liang, H. Feng, Z. Sun, Z. Jiang and W.-D. Li, *Microsyst. Nanoeng.*, 2024, **10**, 49.
50 M. Idrees, S. Ahmed, Z. Mohammed, N. S. Korivi and V. Rangari, *Addit. Manuf.*, 2020, **36**, 101525.
51 J. Chen, P. Wu, F. Bu, Y. Gao, X. Liu and C. Guan, *DeCarbon*, 2023, **2**, 100019.
52 M. S. Carvalho, R. G. Rocha, A. B. Nascimento, D. A. G. Araújo, T. R. L. C. Paixão, O. F. Lopes, E. M. Richter and R. A. A. Muñoz, *Electrochim. Acta*, 2024, **506**, 144995.
53 *Mobile Wireless Middleware, Operating Systems and Applications: 10th International Conference on Mobile Wireless Middleware, Operating Systems and Applications (MOBILWARE 2021)*, ed. D. Tang, J. Zhong and D. Zhou, Springer International Publishing, Cham, 2022.
54 J. C. Ruiz-Morales, A. Tarancón, J. Canales-Vázquez, J. Méndez-Ramos, L. Hernández-Afonso, P. Acosta-Mora, J. R. Marín Rueda and R. Fernández-González, *Energy Environ. Sci.*, 2017, **10**, 846–859.
55 O. Halevi, J. M. R. Tan, P. S. Lee and S. Magdassi, *Adv. Sustainable Syst.*, 2018, **2**, 1700150.
56 W. Y. Lieu, D. Fang, K. J. Tay, X. L. Li, W. C. Chu, Y. S. Ang, D. Li, L. Ang, Y. Wang and H. Y. Yang, *Adv. Mater. Technol.*, 2022, **7**, 2200023.
57 A. Figuerola, D. A. V. Medina, A. J. Santos-Neto, C. P. Cabello, V. Cerdà, G. T. Palomino and F. Maya, *Appl. Mater. Today*, 2019, **16**, 21–27.
58 H. Thakkar, S. Eastman, Q. Al-Naddaf, A. A. Rownaghi and F. Rezaei, *ACS Appl. Mater. Interfaces*, 2017, **9**, 35908–35916.
59 J. Dhainaut, M. Bonneau, R. Ueoka, K. Kanamori and S. Furukawa, *ACS Appl. Mater. Interfaces*, 2020, **12**, 10983–10992.
60 A. D. Salazar-Aguilar, A. Quintanilla, P. López, C. Martínez, S. M. Vega-Díaz, J. A. Casas, P. Miranzo, M. I. Osendi and M. Belmonte, *ACS Appl. Mater. Interfaces*, 2022, **14**, 920–932.
61 Z. Lyu, G. J. H. Lim, R. Guo, Z. Kou, T. Wang, C. Guan, J. Ding, W. Chen and J. Wang, *Adv. Funct. Mater.*, 2019, **29**, 1806658.
62 A. D. Salazar-Aguilar, A. Quintanilla, S. M. Vega-Díaz, J. A. Casas, P. Miranzo, M. I. Osendi and M. Belmonte, *Open Ceram.*, 2021, **5**, 100047.
63 X. Liu, D. Zhao and J. Wang, *Nano-Micro Lett.*, 2024, **16**, 157.
64 H. Molavi, K. Mirzaei, M. Barjasteh, S. Y. Rahnamaee, S. Saeedi, A. Hassanpouryouzband and M. Rezakazemi, *Nano-Micro Lett.*, 2024, **16**, 272.
65 X. Qi, K. Liu and Z. Chang, *Chem. Eng. J.*, 2022, **441**, 135953.
66 M. Saquib, M. Selvakumar, R. Nayak, A. Prakash, Y. N. Sudhakar, S. Senthilkumar and D. K. Bhat, *J. Energy Storage*, 2024, **103**, 114230.
67 T. An, Y. Wang, J. Tang, Y. Wang, L. Zhang and G. Zheng, *J. Colloid Interface Sci.*, 2015, **445**, 320–325.
68 D. Tian, J. Xu, Z. Xie, Z. Yao, D. Fu, Z. Zhou and X. Bu, *Adv. Sci.*, 2016, **3**, 1500283.
69 X. Luo, J. Yu, H. Tang, H. Cai, W. Xiong, K. Zhang, F. Huang and Y. Cao, *FlexMat*, 2024, **1**, 105–115.
70 Y. Xiao, Z. Xie, M. Shen, H. Wang, J. Li, R. Huang and T. Yu, *FlexMat*, 2024, **1**, 193–202.
71 W. Kwak, J. Yin, S. Wang and J. Chen, *FlexMat*, 2024, **1**, 5–22.
72 M. M. Baig, S. A. Khan, H. Ahmad, J. Liang, G. Zhu, H. Pang and Y. Zhang, *FlexMat*, 2024, **1**, 79–99.
73 M. M. Baig, S. A. Khan, H. Ahmad, J. Liang, G. Zhu, H. Pang and Y. Zhang, *FlexMat*, 2024, **1**, 79–99.
74 H. Zhou, S. Gu, Y. Lu, G. Zhang, B. Li, F. Dou, S. Cao, Q. Li, Y. Sun, M. Shakouri and H. Pang, *Adv. Mater.*, 2024, **36**, 2401856.
75 Z. Zhang, H. Yoshikawa and K. Awaga, *Chem. Mater.*, 2016, **28**, 1298–1303.
76 K. Wang, Z. Wang, X. Wang, X. Zhou, Y. Tao and H. Wu, *J. Power Sources*, 2018, **377**, 44–51.
77 M. Lai, D. Zhang, F. Chen, X. Lin, A. Qiu, C. Lei, J. Liang, J. Liang, J. Li, Q. Wang and R. Zeng, *Batteries*, 2023, **9**, 247.
78 Z. Wu, D. Adekoya, X. Huang, M. J. Kiefel, J. Xie, W. Xu, Q. Zhang, D. Zhu and S. Zhang, *ACS Nano*, 2020, **14**, 12016–12026.
79 Y. He, Z. Chang, S. Wu, Y. Qiao, S. Bai, K. Jiang, P. He and H. Zhou, *Adv. Energy Mater.*, 2018, **8**, 1802130.
80 X. Ma, Y. Lou, X.-B. Chen, Z. Shi and Y. Xu, *Chem. Eng. J.*, 2019, **356**, 227–235.
81 Y. Xiang, L. Zhou, P. Tan, S. Dai, Y. Wang, S. Bao, Y. Lu, Y. Jiang, M. Xu and X. Zhang, *ACS Nano*, 2023, **17**, 19275–19287.
82 M. Z. Akram, A. A. Qaiser, N. Abid and M. A. Shehzad, *Mater. Chem. Phys.*, 2025, **340**, 130863.
83 M. A. Abdelkareem, Q. Abbas, E. T. Sayed, N. Shehata, J. B. M. Parambath, A. H. Alami and A. G. Olabi, *Energy*, 2024, **299**, 131127.
84 H. Zhou, P. Wen, X. Chen, N. Zhao, Q. Wang, Z. Ma and M. Kang, *J. Power Sources*, 2024, **601**, 234288.
85 W. Guo, S. Wang, H. Hao, X. Ma, X. Zhao, X. Kong, H. Yan, L. Zhang, R. Liu, X. Li, X. Li, H. Zhu, Y. Li, J. Yin, H. Zhou, D. Zhong and F. Dai, *Inorg. Chem.*, 2023, **62**, 5757–5771.

86 B.-J. Tan, J.-T. Ren, B.-H. Duan, M.-H. Xu, S.-L. Chen, H. Zhang and N. Liu, *Dalton Trans.*, 2022, **51**, 7804–7810.
87 R.-Y. Wang, A.-P. Huang, W.-B. Wang, H.-Z. Sun, B.-S. Teng, Y.-J. Ma and B.-L. Wu, *Solid State Chem.*, 2020, **292**, 121702.
88 B. Chen, X. Zeng, Y. Liu, F. Xiao, M. Huang, K.-B. Tan, D. Cai, J. Huang and J. Zhan, *Chem. Eng. J.*, 2022, **450**, 138470.
89 J. Zhang, B. Jin, X. Li, W. Hao, T. Huang, B. Lei, Z. Guo, J. Shen and R. Peng, *Chem. Eng. J.*, 2021, **404**, 126287.
90 Z. Wang, D. Zhou, D. Liu and B. Zhu, *Food Chem.*, 2023, **418**, 136000.
91 W. Liang, B. Wang, J. Cheng, D. Xiao, Z. Xie and J. Zhao, *J. Hazard. Mater.*, 2021, **401**, 123718.
92 X. Liu, Y. Wu, F. Yang, S. Wang, B. Zhang and L. Wang, *J. Membr. Sci.*, 2021, **626**, 119190.
93 W. Li, B. Yang, R. Pang, L. Zhong and M. Zhang, *ACS Appl. Nano Mater.*, 2023, **6**, 1059–1071.
94 Y. Shi, Q. Chang, T. Song, M. Yin, L. Zhang, X. Cao, Z. Wei and X. Cao, *Chem. Eng. J.*, 2024, **479**, 147394.
95 H. Gao, *Int. J. Hydrogen Energy*, 2022, **47**, 9346–9356.
96 N. Zhang, X. Zhang, Y. Zhu, D. Wang, W. Liu, D. Chen, R. Li and S. Li, *Int. J. Biol. Macromol.*, 2024, **264**, 130625.
97 A. El-Mir, O. Najm, H. El-Hassan, A. El-Dieb and A. Alzamly, *Constr. Build. Mater.*, 2024, **425**, 136061.
98 J. P. Mwizerwa, J. Li, W. Nsengiyumva, C. Li, K. Xu, S. A. Rasaki and C. Liu, *J. Colloid Interface Sci.*, 2025, **696**, 137883.
99 M. Yin, J. Luo, C. Yang, Y. Xue, W. Lu, J. Zhang, Y. Liu, L. Zhang, Y. Zhang, H. Zhang and J. Yu, *Compos. Commun.*, 2025, **54**, 102260.
100 B. Satheesh Kumar, K. R. Roshith, G. Unnikrishnan and K. S. Santhosh Kumar, *Polymer*, 2023, **274**, 125904.
101 J. Liu, J. Wang, L. Zhu, X. Chen, Q. Ma, L. Wang, X. Wang and W. Yan, *Chem. Eng. J.*, 2021, **411**, 128540.
102 Z. Miao, J. Yu, X. Li, Y. Ye, P. Song, P. He, S. Chen and T. Liu, *J. Energy Chem.*, 2025, **104**, 505–513.
103 S. Lin, S. A. Kedzior, J. Zhang, M. Yu, V. Saini, R. P. S. Huynh, G. K. H. Shimizu and M. Trifkovic, *Chem*, 2023, **9**, 2547–2560.
104 H. Wang, Q. Wang, X. Cao, Y. He, K. Wu, J. Yang, H. Zhou, W. Liu and X. Sun, *Adv. Mater.*, 2020, **32**, 2001259.
105 Q. Cheng, F. Wang, Y. Yu, C. Wang, Z. Shao, B. Peng and Y. Guo, *J. Solid State Electrochem.*, 2024, **28**, 2631–2642.
106 J. Zhou, X. Wang, J. Fu, L. Chen, X. Wei, R. Jia and L. Shi, *Small*, 2024, **20**, 2309317.
107 H. Thakkar, S. Eastman, Q. Al-Naddaf, A. A. Rownaghi and F. Rezaei, *ACS Appl. Mater. Interfaces*, 2017, **9**, 35908–35916.
108 J. Lefevere, B. Claessens, S. Mullens, G. Baron, J. Cousin-Saint-Remi and J. F. M. Denayer, *ACS Appl. Nano Mater.*, 2019, **2**, 4991–4999.
109 C. A. Grande, R. Blom, V. Middelkoop, D. Matras, A. Vamvakeros, S. D. M. Jacques, A. M. Beale, M. Di Michiel, K. Anne Andreassen and A. M. Bouzga, *Chem. Eng. J.*, 2020, **402**, 126166.
110 E. R. Kearns, Q. Xia, R. Gillespie, N. Proschogo, P. W. Doheny, M. B. Solomon and D. M. D'Alessandro, *ACS Appl. Mater. Interfaces*, 2023, **15**, 32935–32944.
111 G. J. H. Lim, Y. Wu, B. B. Shah, J. J. Koh, C. K. Liu, D. Zhao, A. K. Cheetham, J. Wang and J. Ding, *ACS Materials Lett.*, 2019, **1**, 147–153.
112 M. Z. Hussain, P. F. Großmann, F. Kohler, T. Kratky, L. Kronthaler, B. Van Der Linden, K. Rodewald, B. Rieger, R. A. Fischer and Y. Xia, *Sol. RRL*, 2022, **6**, 2200552.
113 W. Xi, J. Zhang, Y. Zhang, R. Wang, Y. Gong, B. He, H. Wang and J. Jin, *J. Mater. Chem. A*, 2023, **11**, 7679–7689.
114 H. Zhou, G. Zhu, S. Dong, P. Liu, Y. Lu, Z. Zhou, S. Cao, Y. Zhang and H. Pang, *Adv. Mater.*, 2023, **35**, 2211523.
115 H. R., T. Dhilipkumar, K. V. Shankar, K. P, S. Salunkhe, R. Venkatesan, G. A. Shazly, A. A. Vetcher and S.-C. Kim, *Polymers*, 2024, **16**, 2397.
116 A. Bodin, T. Pietri, C. Celle and J.-P. Simonato, *Mater. Chem. Front.*, 2024, **8**, 3949–3961.
117 A. Czerwiński, M. Słojewska, J. Jurczak, M. Dębowski and E. Zygadło-Monikowska, *Molecules*, 2024, **29**, 4526.
118 F. Cheng, H. Liu and X. Lv, *Adv. Eng. Inform.*, 2025, **65**, 103292.
119 A. A. Pavlovskii, K. Pushnitsa, A. Kosenko, P. Novikov and A. A. Popovich, *Materials*, 2024, **17**, 5904.
120 M. C. Kreider, M. Sefa, J. A. Fedchak, J. Scherschligt, M. Bible, B. Natarajan, N. N. Klimov, A. E. Miller, Z. Ahmed and M. R. Hartings, *Polym. Adv. Technol.*, 2018, **29**, 867–873.
121 T. Wu, X. Huan, X. Jia, G. Sui, L. Wu, Q. Cai and X. Yang, *Composites, Part B*, 2022, **233**, 109658.
122 J. W. Oh, S. Lee, H. Han, O. Allam, J. I. Choi, H. Lee, W. Jiang, J. Jang, G. Kim, S. Mun, K. Lee, Y. Kim, J. W. Park, S. Lee, S. S. Jang and C. Park, *Light Sci. Appl.*, 2023, **12**, 226.
123 R. Simões, J. Rodrigues, C. M. Granadeiro, L. Rino, V. Neto, T. Monteiro and G. Gonçalves, *Mater. Today Chem.*, 2023, **29**, 101436.
124 A. Pustovarenko, B. Seoane, E. Abou-Hamad, H. E. King, B. M. Weckhuysen, F. Kapteijn and J. Gascon, *Mater. Adv.*, 2021, **2**, 2739–2749.
125 V. T. Huong, B. V. Duc, N. T. An, T. T. P. Anh, T. M. Aminabhavi, Y. Vasseghian and S.-W. Joo, *Chem. Eng. J.*, 2024, **483**, 149277.
126 S. D. Perera, R. M. Johnson, R. Pawle, J. Elliott, T. M. Tran, J. Gonzalez, J. Huffstetler, L. C. Ayers, V. Ganesh, M. C. Senarathna, K. P. Cortés-Guzmán, S. Dube, S. Springfield, L. F. Hancock, B. R. Lund and R. A. Smaldone, *ACS Appl. Mater. Interfaces*, 2024, **16**, 10795–10804.
127 C.-E. Choi, A. Chakraborty, H. Adzija, Y. Shamiya, K. Hijazi, A. Coyle, A. Rizkalla, D. W. Holdsworth and A. Paul, *Gels*, 2023, **9**, 923.
128 J. Liu, Y. Liu, C. Deng, K. Yu, X. Fan, W. Zhang, Y. Tao, H. Hu, L. Deng and W. Xiong, *Adv. Mater. Technol.*, 2022, **7**, 2101230.
129 A. I. Cherevko, I. A. Nikovskiy, Y. V. Nelyubina, K. M. Skupov, N. N. Efimov and V. V. Novikov, *Polymers*, 2021, **13**, 3881.

130 R. Li, S. Yuan, W. Zhang, H. Zheng, W. Zhu, B. Li, M. Zhou, A. Wing-Keung Law and K. Zhou, *ACS Appl. Mater. Interfaces*, 2019, **11**, 40564–40574.
131 S. Lawson, X. Li, H. Thakkar, A. A. Rownaghi and F. Rezaei, *Chem. Rev.*, 2021, **121**, 6246–6291.
132 Q. Liu, L. Yang, Z. Mei, Q. An, K. Zeng, W. Huang, S. Wang, Y. Sun and H. Guo, *Energy Environ. Sci.*, 2024, **17**, 780–790.
133 X. Guo, H. Xu, Y. Tang, Z. Yang, F. Dou, W. Li, Q. Li and H. Pang, *Adv. Mater.*, 2024, **36**, 2408317.
134 J. E. Sánchez-Velandia, F. Esteve, M. Maireles, D. Iglesias, N. Martín, M. Zanatta, V. Sans, F. G. Cirujano and E. García-Verdugo, *J. CO_2 Util.*, 2023, **78**, 102636.
135 Z. Wang, J. Wang, M. Li, K. Sun and C. Liu, *Sci. Rep.*, 2014, **4**, 5939.
136 Z. Shi, C. Xu, F. Chen, Y. Wang, L. Li, Q. Meng and R. Zhang, *RSC Adv.*, 2017, **7**, 49947–49952.
137 S. Waheed, M. Rodas, H. Kaur, N. L. Kilah, B. Paull and F. Maya, *Appl. Mater. Today*, 2021, **22**, 100930.
138 S. Lawson, Q. Al-Naddaf, A. Krishnamurthy, M. St. Amour, C. Griffin, A. A. Rownaghi, J. C. Knox and F. Rezaei, *ACS Appl. Mater. Interfaces*, 2018, **10**, 19076–19086.
139 S. Lawson, M. Snarzyk, D. Hanify, A. A. Rownaghi and F. Rezaei, *Ind. Eng. Chem. Res.*, 2020, **59**, 7151–7160.
140 S. Lawson, A.-A. Alwakwak, A. A. Rownaghi and F. Rezaei, *ACS Appl. Mater. Interfaces*, 2020, **12**, 56108–56117.
141 W. Liu, O. Erol and D. H. Gracias, *ACS Appl. Mater. Interfaces*, 2020, **12**, 33267–33275.
142 F. Xie, X. Cui, X. Zhi, D. Yao, B. Johannessen, T. Lin, J. Tang, T. B. F. Woodfield, L. Gu and S.-Z. Qiao, *Nat. Synth.*, 2023, **2**, 129–139.
143 Z. Liu, X. Xia, W. Li, L. Xiao, X. Sun, F. Luo, Q. Chen and Q. Qian, *Materials*, 2020, **13**, 4403.
144 D. Liu, P. Jiang, X. Li, J. Liu, L. Zhou, X. Wang and F. Zhou, *Chem. Eng. J.*, 2020, **397**, 125392.
145 J. Huang and P. Wu, *Nano-Micro Lett.*, 2021, **13**, 15.
146 J. Duan, Q. Li, W. Xu, X. Hu, Y. Wang, S. M. Valdez, Z. Qiang, Y. Liao, J. Wen, C. Ye and M. Zhu, *ACS Appl. Polym. Mater.*, 2024, **6**, 1900–19104.
147 M. Del Rio, M. Villar, S. Quesada, G. Turnes Palomino, L. Ferrer and C. Palomino Cabello, *Appl. Mater. Today*, 2021, **24**, 101130.
148 M. Bauzá, N. Munar, A. Figuerola, G. Turnes Palomino and C. Palomino Cabello, *J. Water Proc. Eng.*, 2024, **58**, 104890.
149 M. A. Vargas-Muñoz, C. Palomino, G. Turnes and E. Palacio, *J. Environ. Chem. Eng.*, 2023, **11**, 110503.
150 D. Barzallo, A. Están, N. Crespí, C. Palomino, G. Turnes, E. Palacio and L. Ferrer, *Talanta*, 2024, **273**, 125897.
151 N. Fijoł, A. Mautner, E. S. Grape, Z. Bacsik, A. K. Inge and A. P. Mathew, *J. Mater. Chem. A*, 2023, **11**, 12384–12394.
152 J. Zhao, Y. Zhang, H. Lu, Y. Wang, X. D. Liu, H. Maleki Kheimeh Sari, J. Peng, S. Chen, X. Li, Y. Zhang, X. Sun and B. Xu, *Nano Lett.*, 2022, **22**, 1198–1206.
153 N. R. Catarineu, D. Lin, C. Zhu, D. I. Oyarzun and Y. Li, *Chem. Eng. J.*, 2023, **465**, 142544.
154 Y.-P. Chuang, C.-H. Shen, H.-J. Hsu, Y.-Z. Su, S.-C. Yang, S.-S. Yu and C.-W. Kung, *ACS Appl. Nano Mater.*, 2023, **6**, 19701–19709.
155 H. Zhou, Y. Sun, H. Yang, Y. Tang, Y. Lu, Z. Zhou, S. Cao, S. Zhang, S. Chen, Y. Zhang and H. Pang, *Adv. Sci.*, 2023, **10**, 2303636.
156 Z. Lyu, G. J. H. Lim, R. Guo, Z. Kou, T. Wang, C. Guan, J. Ding, W. Chen and J. Wang, *Adv. Funct. Mater.*, 2019, **29**, 1806658.
157 Z. Lyu, G. J. H. Lim, R. Guo, Z. Pan, X. Zhang, H. Zhang, Z. He, S. Adams, W. Chen, J. Ding and J. Wang, *Energy Storage Mater.*, 2020, **24**, 336–342.
158 C. Li, S. Deng, W. Feng, Y. Cao, J. Bai, X. Tian, Y. Dong and F. Xia, *Small*, 2023, **19**, 2300066.
159 E. Zhang, X. Hu, L. Meng, M. Qiu, J. Chen, Y. Liu, G. Liu, Z. Zhuang, X. Zheng, L. Zheng, Y. Wang, W. Tang, Z. Lu, J. Zhang, Z. Wen, D. Wang and Y. Li, *J. Am. Chem. Soc.*, 2022, **144**, 18995–19007.
160 W. Xi, J. Zhang, Y. Zhang, R. Wang, Y. Gong, B. He, H. Wang and J. Jin, *J. Mater. Chem. A*, 2023, **11**, 7679–7689.
161 M. Idrees, S. Batool, W. Hu and D. Chen, *Small*, 2024, **20**, 2402266.
162 S. Batool, M. Idrees and J. Xu, *J. Power Sources*, 2024, **624**, 235570.
163 H. Lu, J. Hu, K. Zhang, J. Zhao, S. Deng, Y. Li, B. Xu and H. Pang, *Adv. Mater.*, 2024, **36**, 2309753.